Agenzia Nazionale per le Nuove Tecnologie,
l'Energia e lo Sviluppo Economico Sostenibile

Ministero dello Sviluppo Economico

RICERCA DI SISTEMA ELETTRICO

Documento CERSE-UNIBO RL 1258/2010

Development of a Model for Core Dynamics-Neutronics

S. Dulla, P. Ravetto, S. Han, F. Alcaro

Report RdS/2010/108

DEVELOPMENT OF A MODEL FOR CORE DYNAMICS-NEUTRONICS

S. Dulla, P. Ravetto, S. Han, F. Alcaro

Settembre 2010

Report Ricerca di Sistema Elettrico
Accordo di Programma Ministero dello Sviluppo Economico – ENEA
Area: Produzione e fonti energetiche
Tema: Nuovo Nucleare da Fissione

Responsabile Tema: Stefano Monti, ENEA

CIRTEN

CONSORZIO INTERUNIVERSITARIO

PER LA RICERCA TECNOLOGICA NUCLEARE

POLITECNICO DI TORINO

DIPARTIMENTO DI ENERGETICA

Development of a model for core dynamics - Neutronics

CIRTEN-POLITO RL 1258/2010

AUTORI

S. Dulla
P. Ravetto
S. Han
F. Alcaro

TORINO, LUGLIO 2010

Lavoro svolto in esecuzione della linea progettuale LP3 punto F2 - AdP ENEA MSE del 21/06/07
Tema 5.2.5.8 – “Nuovo Nucleare da Fissione”.

Introduzione e sommario del lavoro

Lo sviluppo di un modello computazionale per il calcolo neutronico di un sistema innovativo richiede la messa a punto di un algoritmo per la soluzione delle equazioni di bilancio in geometria pluridimensionale. Nel primo anno di questa attività di ricerca è stato sviluppato un modulo di calcolo per la soluzione delle equazioni della diffusione multigruppi in geometria cartesiana multidimensionale. Sono stati adottati diversi approcci numerici per studiarne l'efficienza e le prestazioni. In particolare, accanto ad un approccio alle differenze finite classico, da utilizzare principalmente come riferimento perché computazionalmente troppo costoso, si è voluto sviluppare sia un metodo nodale adatto a calcoli parametrici veloci ma accurati che un nuovo metodo agli elementi di contorno.

Nel corso dell'attività di ricerca del secondo anno, il lavoro si è sviluppato allo scopo di conseguire principalmente due obiettivi. In una prima fase il modulo numerico sviluppato nell'anno precedente è stato sottoposto a verifiche mediante confronti con vari benchmark analitici e numerici. Ciò ha permesso di studiare i vari aspetti connessi alle limitazioni degli approcci computazionali adottati. E' stata inoltre sviluppata un'analisi comparativa dei costi di calcolo.

E' noto che i metodi a maglia larga, quali quelli nodali e agli elementi di contorno, possono presentare diversi problemi di instabilità e di non convergenza quando applicati con discretizzazioni spaziali non consistenti. Si è pertanto voluto approfondire tale aspetto nel corso di questa parte dell'attività di ricerca. Questo lavoro ha permesso di arrivare ad interessanti valutazioni che hanno portato a un lavoro scientifico pubblicato e recentemente presentato alla conferenza annuale dell'American Nuclear Society. Questa analisi ha messo chiaramente in luce la necessità di una strutturazione consistente della discretizzazione spaziale per evitare problemi numerici che possono generare soluzioni non fisiche o produrre risultati insoddisfacenti.

In un secondo campo di attività si è dato inizio allo studio della possibilità di estendere il modulo computazionale a problemi dipendenti dal tempo. Questo era stato fissato come uno degli obiettivi iniziali del lavoro. In questa fase si è studiata a fondo la possibilità di accoppiare un modulo di calcolo statico ad un modulo di cinetica puntiforme nell'ambito di una procedura quasi-statica, utilizzando il modulo statico per l'aggiornamento della forma della popolazione neutronica, in uno schema fattorizzato forma-ampiezza. Questo lavoro è stato svolto anche nell'ambito di collaborazioni internazionali avviate con ricercatori sia dell'Université Libre de Bruxelles che dell'Ecole Polytechnique de Montréal. In questa fase del lavoro è stato messo a punto uno strumento informatico di accoppiamento fra il modulo di calcolo di forma e quello per la valutazione delle ampiezze. I risultati sono stati particolarmente promettenti e hanno portato alla pubblicazione di un lavoro su rivista scientifica.

Il rapporto che segue comprende una prima parte in cui viene sommariamente descritto il modulo statico di neutronica pluridimensionale nelle sue varie articolazioni numeriche come sviluppato nella prima parte di questa attività. Successivamente viene discusso in dettaglio il problema della validazione e lo studio delle prestazioni. Sono presentati i risultati dell'analisi comparativa dei costi computazionali. Una parte consistente è dedicata allo studio del problema di stabilità e di convergenza degli algoritmi a maglia larga. Vengono illustrati gli aspetti connessi alla necessità di adottare una discretizzazione spaziale coerente, soprattutto quando venga scelto l'algoritmo a elementi di contorno. La parte finale del rapporto è dedicata allo studio dello schema quasistatico e alla possibilità di accoppiamento di un modulo statico con un modulo di cinetica.

L'attività di ricerca che si sta ora avviando riguarda la messa a punto e la validazione di un modulo completo di dinamica. Questo prevede quindi lo sviluppo completo di uno schema quasi-statico e l'accoppiamento con un modulo di calcolo termoidraulico. Ciò permetterà la simulazione completa del comportamento dinamico di un sistema, tenendo conto in modo consistente degli effetti di controreazione termica.

Quest'ultima attività è stata recentemente discussa in due incontri di lavoro che si sono svolti presso il Politecnico di Torino e presso la sede ENEA di Bologna.

Torino, settembre 2010

Development of a model for core dynamics - Neutronics

Contribution from Politecnico di Torino

This material has been partially published in:

- Song H., Dulla S., Ravetto P., Performance and convergence issues of coarse mesh methods for diffusion calculations, *Transactions of the American Nuclear Society*, **102**, 525-527, 2010.

- Alcaro F, Dulla S., Marleau G., Mund E.H., Ravetto P., Development of dynamic models for neutron transport caclulations, *Il Nuovo Cimento*, **33C**, 13-20, 2010.

Chapter 1

Boundary elements method for neutron diffusion problems and convergence

Contributors: Song Han, Sandra Dulla, Piero Ravetto (Politecnico di Torino)

1.1 Introduction

Boundary Elements Methods (BEM) applied for neutron diffusion problems has been investigated for some time recently. However, this technique has some difficulties to display its excellent features which are shown in other fields due to some special reasons of the diffusion model. Firstly, numerical integrations on the boundary element has to be applied because they cannot normally be performed analytically. A significant error can be introduced by such approach because the integrand is singular in the domain. Secondly, volume integral of neutron external source term in the neutron diffusion boundary integrated equations is hard to be evaluated accurately. This requires some proper approximation on the spatial distribution. In particular for critical calculations in multi-group diffusion problems for reactor systems, the fission source brings forward another problem once it is considered as a given source in the iterative process. The advantage of being assimilated to an external source is that the response matrix is calculated only once before the critical iteration process, while the drawback is the problem of the volume integral and its spatial distribution.

1.2 Algorithm

Owing to these difficulties, an algorithm for the spatial treatment of the fission source as an external source is developed and investigated. It is based on the multi-group diffusion equations in two-dimensional (2D) Cartesian geometry:

$$-\nabla D^g \nabla \phi_g(\mathbf{r}) + \Sigma_r^g \phi_g(\mathbf{r}) = \sum_{g'=1, g' \neq g}^{G} \Sigma_s^{g' \to g} \phi_{g'}(\mathbf{r}) + \frac{1}{k} \chi^g \sum_{g'=1}^{G} \nu \Sigma_f^{g'} \phi_{g'}(\mathbf{r}), \quad g = 1, 2, \ldots, G \ , \qquad (1.1)$$

where
D^g, diffusion coefficient of g^{th} group;

$\Sigma_r^g \equiv \Sigma_a^g + \Sigma_s^g - \Sigma_s^{g\to g'}$, removal cross section of g^{th} group ;
$\Sigma_s^{g\to g'}$, scattering cross section from g^{th} group to g'^{th} group ;
$\nu\Sigma_f^{g'}$, neutron number per fission times fission cross section of g'^{th} group;
χ^g, neutron spectrum of g^{th} group;
$\phi_g(\mathbf{r})$, neutron flux density of g^{th} group;
$s_g(\mathbf{r})$, neutron independent source density of g^{th} group;
k_{eff}, effective multiplication constant.

Equation (1.1) can be cast into matrix form as

$$\left(\nabla^2\mathbf{I} + \mathbf{Q}\right)\boldsymbol{\phi}(\mathbf{r}) + \mathbf{q}(\mathbf{r}) = 0, \tag{1.2}$$

where ϕ and $\mathbf{q}$ are G-dimensional vectors of the neutron group fluxes and group external sources, respectively. At first, we need to define the removal cross-section operator, $\mathbf{R}$, assuming there is no neutron scattering from a lower energy group to a higher one, as:

$$\mathbf{R} = \begin{bmatrix} -\dfrac{\Sigma_r^1}{D^1} & 0 & \dots & 0 \\ \dfrac{\Sigma_s^{1\to 2}}{D^2} & -\dfrac{\Sigma_r^2}{D^2} & \dots & 0 \\ \vdots & \vdots & \ddots & \vdots \\ \dfrac{\Sigma_s^{1\to G}}{D^G} & \dfrac{\Sigma_s^{2\to G}}{D^G} & \dots & -\dfrac{\Sigma_r^G}{D^G} \end{bmatrix}$$

and the fission operator, $\mathbf{F}$, as

$$\mathbf{F} = \begin{bmatrix} \dfrac{\chi^1}{D^1}\nu\Sigma_f^1 & \dfrac{\chi^1}{D^1}\nu\Sigma_f^2 & \dots & \dfrac{\chi^1}{D^1}\nu\Sigma_{fG} \\ \dfrac{\chi^2}{D^2}\nu\Sigma_f^1 & \dfrac{\chi^2}{D^2}\nu\Sigma_f^2 & \dots & \dfrac{\chi^2}{D^2}\nu\Sigma_f^G \\ \vdots & \vdots & \ddots & \vdots \\ \dfrac{\chi^G}{D^G}\nu\Sigma_f^1 & \dfrac{\chi^G}{D^G}\nu\Sigma_f^2 & \dots & \dfrac{\chi^G}{D^G}\nu\Sigma_f^G \end{bmatrix}. \tag{1.3}$$

Then, $\mathbf{Q}$ and $\mathbf{q}$ can be defined according to different options for critical problems. In a previous model, they are defined as:

$$\mathbf{Q} = \mathbf{R} + \frac{1}{k}\mathbf{F}, \quad \mathbf{q} = 0. \tag{1.4}$$

The advantage is that the fission operator is included in $\mathbf{Q}$, so that the BEM algorithm is naturally adopted on the fission source term. However, the drawback is that $\mathbf{Q}$ has to be updated at each step of the iteration procedure because the multiplication constant, k, is included in the matrix.

As an alternative option, we define:

$$\mathbf{Q} = \mathbf{R}, \quad \mathbf{q} = \frac{1}{k}\mathbf{F}\boldsymbol{\phi}. \tag{1.5}$$

The advantage of this option is connected to the fact that the fission operator is excluded from $\mathbf{Q}$, so that the matrix is only calculated once before starting the iteration procedure, but the drawback is that fission source term as an external source has to be evaluated by some special treatment which might be complicated and not very efficient.

Table 1.1: Two options on the construction of $\mathbf{Q}$ and $\mathbf{q}$ for critical problems

	Previous model	New model
Model	$\mathbf{Q} = \mathbf{R} + \frac{1}{k}\mathbf{F}$; $\mathbf{q} = 0$.	$\mathbf{Q} = \mathbf{R}$; $\mathbf{q} = \frac{1}{k}\mathbf{F}\phi$.
Fission source approximation	Fission x-section is included in RM so that BEM algorithm is well adopted on fission source term.	Fission x-section is excluded from RM so that volume approximation has to be treated specially.
Response Matrix (RM) reconstruction	RM is reconstructed during iteration procedure so that a large amount of CPU time is need to calculate RM.	RM is constructed before iteration procedure so that RM is calculated once.

Actually, in the case of a critical problem, Eq. (1.2) becomes an eigenvalue equation,

$$\mathbf{Q}\sigma = \lambda\sigma,$$

where $\mathbf{S}$ is defined as the matrix which has the normalized eigenvectors σ_h as its columns. Thus, the following equality is verified, by left multiplication by $\mathbf{S}^{-1}$, where $\mathbf{S}$ is defined as

$$\mathbf{S}^{-1}\mathbf{Q}\mathbf{S} = \mathbf{\Lambda},$$

and $\mathbf{\Lambda} = \mathrm{diag}[\lambda_1, ..., \lambda_G]$. Equation (**??**) becomes

$$\nabla^2\boldsymbol{\psi}(\mathbf{r}) + \mathbf{\Lambda}\boldsymbol{\psi}(\mathbf{r}) + \boldsymbol{\eta}(\mathbf{r}) = 0$$

where

$$\boldsymbol{\phi}(\mathbf{r}) = \mathbf{S}\boldsymbol{\psi}(\mathbf{r}), \mathbf{q}(\mathbf{r}) = \mathbf{S}\boldsymbol{\eta}(\mathbf{r}).$$

In the diagonal matrix, $\mathbf{\Lambda} = \mathrm{diag}[\lambda_1, ..., \lambda_G]$, λ_h are the G real and distinct eigenvalues of $\mathbf{Q}$. Such treatment allows us to have G uncoupled equations as separate single group equations. The corresponding *Green's* fundamental solutions of the following equations:

$$\nabla^2\tilde{\psi}_h(\mathbf{r}, \mathbf{r}') - \gamma_h^2\tilde{\psi}_h(\mathbf{r}, \mathbf{r}') + \delta(\mathbf{r} - \mathbf{r}') = 0, \qquad h = 1, 2, \ldots, G,$$

are easily found out as:

$$\tilde{\psi}_h(\mathbf{r}, \mathbf{r}') = \frac{1}{2\pi}K_0(\gamma_h|\mathbf{r} - \mathbf{r}'|) \ ,$$

together with their derivatives,

$$\frac{\partial\tilde{\psi}_h(\mathbf{r}'_\Gamma)}{\partial\mathbf{n}'} = \frac{\gamma_h}{2\pi}K_1(\gamma_h|\mathbf{r} - \mathbf{r}'|)\frac{(\mathbf{r} - \mathbf{r}')\cdot\mathbf{n}'}{|\mathbf{r} - \mathbf{r}'|}, \tag{1.6}$$

where the functions $K_0(x)$ and $K_1(x)$ are the modified *Bessel functions* of second the kind, 0^{th} and 1^{st} order. Here, $\gamma_h^2 = -\lambda$ is always negative due to the special feature of $\mathbf{\Lambda}$. Boundary integrated equations can be generated, obtaining

$$c(\mathbf{r})\psi_h(\mathbf{r}) + \int_\Gamma [\frac{\tilde{\psi}_h(\mathbf{r}, \mathbf{r}'_\Gamma)}{\partial\mathbf{n}'_\Gamma}\psi_h(\mathbf{r}'_\Gamma) - \tilde{\psi}_h(\mathbf{r}, \mathbf{r}'_\Gamma)\frac{\partial\psi_h(\mathbf{r}'_\Gamma)}{\partial\mathbf{n}'_\Gamma}]d\Gamma' = \int_\Omega \tilde{\psi}_h(\mathbf{r}, \mathbf{r}')\eta_h(\mathbf{r}')d\Omega' \ . \tag{1.7}$$

By left multiplying Eq. (1.7) written in matrix form by $\mathbf{S}$, and taking $\mathbf{r}$ on the boundary as $\mathbf{r} = \mathbf{r}_\Gamma$, one gets the multi-group boundary integrated equations that can be explicitly written down as:

$$\begin{aligned}
&\frac{1}{2}c(\mathbf{r}_\Gamma)J_g^+(\mathbf{r}_\Gamma) + \sum_{g'=1}^{G}\int_\Gamma \tilde{J}_{gg'}^+(\mathbf{r}_\Gamma,\mathbf{r}'_\Gamma)J_{g'}^+(\mathbf{r}'_\Gamma)d\Gamma' \\
&\qquad = -\frac{1}{2}c(\mathbf{r}_\Gamma)J_g^-(\mathbf{r}_\Gamma) + \sum_{g'=1}^{G}\int_\Gamma \tilde{J}_{gg'}^-(\mathbf{r}_\Gamma,\mathbf{r}'_\Gamma)J_{g'}^-(\mathbf{r}'_\Gamma)d\Gamma' + \frac{1}{4}\sum_{g'=1}^{G}\int_\Omega \tilde{\Psi}_{gg'}(\mathbf{r}_\Gamma,\mathbf{r}')q_{g'}(\mathbf{r}')d\Omega' \ , \\
&\qquad g = 1,2,\ldots,G \ ,
\end{aligned} \tag{1.8}$$

where

$$\tilde{\Psi}_{gg'}(\mathbf{r},\mathbf{r}'_\Gamma) = \sum_{h=1}^{G}\sigma_{gh}\tilde{\psi}_h(\mathbf{r},\mathbf{r}'_\Gamma)\sigma^*_{hg'} \tag{1.9}$$

and

$$\begin{aligned}
J_g^\pm(\mathbf{r}_\Gamma) &= \frac{1}{4}\boldsymbol{\phi}(\mathbf{r}_\Gamma) \mp \frac{1}{2}D^g\frac{\partial\boldsymbol{\phi}(\mathbf{r}_\Gamma)}{\partial\mathbf{n}_\Gamma} \ , \\
\tilde{J}_{gg'}^\pm(\mathbf{r}_\Gamma,\mathbf{r}'_\Gamma) &= \frac{1}{4D^{g'}}\tilde{\Psi}(\mathbf{r}_\Gamma,\mathbf{r}'_\Gamma) \pm \frac{1}{2}\frac{\partial\tilde{\Psi}(\mathbf{r}_\Gamma,\mathbf{r}'_\Gamma)}{\partial\mathbf{n}'_\Gamma} \ .
\end{aligned} \tag{1.10}$$

Here, $J_g^\pm(\mathbf{r}_\Gamma)$ takes the definition of neutron partial currents related to fluxes. Therefore, they have the physical meaning of incoming or outgoing currents. Thus, in principle, Equation (1.8) can be solved if the incoming currents $J_g^-(\mathbf{r}_\Gamma)$ and the source term $q_g(\mathbf{r})$ are supposed to be given. The outgoing currents, $J_g^+(\mathbf{r}_\Gamma)$, can be consequently determined on the boundary.

Till now the entire theoretical derivation of the boundary integrated equations has been illustrated. In order to implement Equation (1.8) numerically, a special treatment on the volume integrals of the source term has to be introduced and then the boundary has to be discretized following the BEM algorithm. These numerical treatments play a key role in the BEM application on the neutron diffusion critical problems as far as the behaviors of convergence and precision are concerned.

1.2.1 Reduction of the volume integrals of the source term

In principle, it is normally impossible to obtain the distribution of the neutron source containing fission contribution in the domain analytically, because it is unavoidably determined by the spatial flux distribution which is actually the unknown of our problem. However, one may firstly reduce the integrals involving $q_{g'}(\mathbf{r}')$ in Equation (1.8) into a boundary integrated form,

$$\begin{aligned}
\int_\Omega \tilde{\Psi}_{gg'}(\mathbf{r}_\Gamma,\mathbf{r}')q_{g'}(\mathbf{r}')d\Omega' = -\sum_{h=1}^{G}\frac{\sigma_{gh}\sigma_{hg'}}{B_h^2}\Big\{&c(\mathbf{r}_\Gamma)q_{g'}(\mathbf{r}_\Gamma) + \int_\Omega \tilde{\psi}_h(\mathbf{r}_\Gamma,\mathbf{r}')\nabla^2 q_{g'}(\mathbf{r}')d\Omega' \\
&+ \int_\Gamma [\frac{\tilde{\psi}_h(\mathbf{r}_\Gamma,\mathbf{r}'_\Gamma)}{\partial\mathbf{n}'_\Gamma}q_{g'}(\mathbf{r}'_\Gamma) - \tilde{\psi}_h(\mathbf{r}_\Gamma,\mathbf{r}'_\Gamma)\frac{\partial q_{g'}(\mathbf{r}'_\Gamma)}{\partial\mathbf{n}'_\Gamma}]d\Gamma'\Big\} , \\
&h = 1,2,\ldots,G.
\end{aligned} \tag{1.11}$$

At the right-hand side of Equation (1.11), a new domain integral in which the integrand contains the term, $\nabla^2 q_g(\mathbf{r})$, is still to be handled. Fortunately, if $\nabla^2 q_{g'}(\mathbf{r}') \equiv 0$ is satisfied, which implies $q_g(\mathbf{r})$ can be either spatially constant or 1^{st}-order polynomials in the domain, the integral vanishes. Then,

Equation (1.11) becomes a pure boundary integrated equation

$$\int_{\Omega} \tilde{\Psi}_{gg'}(\mathbf{r}_\Gamma, \mathbf{r}') q_{g'}(\mathbf{r}') d\Omega' = -\sum_{h=1}^{G} \frac{\sigma_{gh}\sigma_{hg'}}{B_h^2} \left\{ c(\mathbf{r}_\Gamma) q_{g'}(\mathbf{r}_\Gamma) + \int_\Gamma \left[\frac{\tilde{\psi}_h(\mathbf{r}_\Gamma, \mathbf{r}'_\Gamma)}{\partial \mathbf{n}'_\Gamma} q_{g'}(\mathbf{r}'_\Gamma) - \tilde{\psi}_h(\mathbf{r}_\Gamma, \mathbf{r}'_\Gamma) \frac{\partial q_{g'}(\mathbf{r}'_\Gamma)}{\partial \mathbf{n}'_\Gamma} \right] d\Gamma' \right\},$$
$$h = 1, 2, \ldots, G, \tag{1.12}$$

Similarly, if we set $\nabla^2 \hat{q}_{g'}(\mathbf{r}') = \nabla^4 q_{g'}(\mathbf{r}') \equiv 0$, the domain integral at the right-hand side of Equation (1.11) can be further reduced to another boundary integrated form,

$$\int_{\Omega} \tilde{\psi}_{gg'}(\mathbf{r}_\Gamma, \mathbf{r}') \nabla^2 q_{g'}(\mathbf{r}') d\Omega' = -\frac{1}{B_h^2} \left\{ c(\mathbf{r}_\Gamma) \hat{q}_{g'}(\mathbf{r}_\Gamma) + \int_\Gamma \left[\frac{\tilde{\psi}_h(\mathbf{r}_\Gamma, \mathbf{r}'_\Gamma)}{\partial \mathbf{n}'_\Gamma} \hat{q}_{g'}(\mathbf{r}'_\Gamma) - \tilde{\psi}_h(\mathbf{r}_\Gamma, \mathbf{r}'_\Gamma) \frac{\partial \hat{q}_{g'}(\mathbf{r}'_\Gamma)}{\partial \mathbf{n}'_\Gamma} \right] d\Gamma' \right\},$$
$$h = 1, 2, \ldots, G, \tag{1.13}$$

Theoretically, the reduction can be continued further, which provides the possibility of higher order approximations on the source term $q_g(\mathbf{r})$, if necessary.

1.2.2 Boundary discretization of the boundary integrated equations

In this section the discretization of the boundary leading to boundary elemented equations is described. It is assumed that the domain is rectangular in 2D geometry. As shown in Figure (1.1), each side is taken as orthogonal to either the x- or the y-axis. Thus, The boundary Γ can be divided into I straight line segments each of length d_i. After denoting the two extremes, $\mathbf{r}_{\Gamma,i-\frac{1}{2}}$ and $\mathbf{r}_{\Gamma,i+\frac{1}{2}}$, and the middle point, $\mathbf{r}_{\Gamma,i}$, of the ith boundary element, a local dimensionless coordinate τ is introduced to identify each point $\mathbf{r}$ along Γ_i as

$$\mathbf{r}_{\Gamma_i}(\tau) = \mathbf{r}_{\Gamma,i} + \frac{\tau}{2}(\mathbf{r}_{\Gamma,i+\frac{1}{2}} - \mathbf{r}_{\Gamma,i-\frac{1}{2}}), \qquad -1 \le \tau \le 1. \tag{1.14}$$

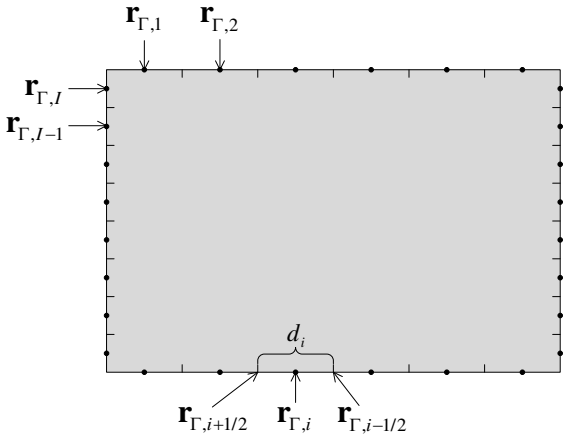

Figure 1.1: Boundary element discretization in 2D geometry.

Thus, it is assumed within each boundary element that

$$\begin{cases} J_g^{\pm}\left[\mathbf{r}_{\Gamma_i}(\tau)\right] = J_{g,i}^{\pm} \\ q_g\left[\mathbf{r}_{\Gamma_i}(\tau)\right] = q_{g,i} \\ \dfrac{\partial q_g}{\partial \mathbf{n}_\Gamma}\left[\mathbf{r}_{\Gamma_i}(\tau)\right] = \left[\dfrac{\partial q_g}{\partial \mathbf{n}_\Gamma}\right]_i \quad , \qquad \mathbf{r}_\Gamma \in \Gamma_i \\ \hat{q}_g\left[\mathbf{r}_{\Gamma_i}(\tau)\right] = \hat{q}_{g,i} \\ \dfrac{\partial \hat{q}_g}{\partial \mathbf{n}_\Gamma}\left[\mathbf{r}_{\Gamma_i}(\tau)\right] = \left[\dfrac{\partial \hat{q}_g}{\partial \mathbf{n}_\Gamma}\right]_i \end{cases}$$

The expressions denote that all terms above within each boundary element take constant values. Therefore, the boundary integrals are approximated by finite sums as

$$\begin{cases} \displaystyle\int_\Gamma \tilde{J}_{gg'}^{\pm}(\mathbf{r}_\Gamma, \mathbf{r}'_\Gamma) J_{g'}^{\pm}(\mathbf{r}'_\Gamma) d\Gamma' \cong \sum_{j=1}^{I} \left\{ J_{g',j}^{\pm} \frac{d_j}{2} \int_{-1}^{1} \tilde{J}_{gg'}^{\pm}\left[\mathbf{r}_{\Gamma,i}, \mathbf{r}_{\Gamma_j}(\tau)\right] d\tau \right\} \\ \displaystyle\int_\Gamma \frac{\partial \tilde{\psi}_h(\mathbf{r}_\Gamma, \mathbf{r}'_\Gamma)}{\partial \mathbf{n}'_\Gamma} q_{g'}(\mathbf{r}'_\Gamma) d\Gamma' \cong \sum_{j=1}^{I} \left\{ q_{g',j} \frac{d_j}{2} \int_{-1}^{1} \frac{\partial \tilde{\psi}_h}{\partial \mathbf{n}'_\Gamma}\left[\mathbf{r}_{\Gamma,i}, \mathbf{r}_{\Gamma_j}(\tau)\right] d\tau \right\} \\ \displaystyle\int_\Gamma \tilde{\psi}_h(\mathbf{r}_\Gamma, \mathbf{r}'_\Gamma) \frac{\partial q_{g'}(\mathbf{r}'_\Gamma)}{\partial \mathbf{n}'_\Gamma} d\Gamma' \cong \sum_{j=1}^{I} \left\{ \left[\frac{\partial q_{g'}}{\partial \mathbf{n}_\Gamma}\right]_j \frac{d_j}{2} \int_{-1}^{1} \tilde{\psi}_h\left[\mathbf{r}_{\Gamma,i}, \mathbf{r}_{\Gamma_j}(\tau)\right] d\tau \right\} \\ \displaystyle\int_\Gamma \frac{\partial \tilde{\psi}_h(\mathbf{r}_\Gamma, \mathbf{r}'_\Gamma)}{\partial \mathbf{n}'_\Gamma} \hat{q}_{g'}(\mathbf{r}'_\Gamma) d\Gamma' \cong \sum_{j=1}^{I} \left\{ \hat{q}_{g',j} \frac{d_j}{2} \int_{-1}^{1} \frac{\partial \tilde{\psi}_h}{\partial \mathbf{n}'_\Gamma}\left[\mathbf{r}_{\Gamma,i}, \mathbf{r}_{\Gamma_j}(\tau)\right] d\tau \right\} \\ \displaystyle\int_\Gamma \tilde{\psi}_h(\mathbf{r}_\Gamma, \mathbf{r}'_\Gamma) \frac{\partial \hat{q}_{g'}(\mathbf{r}'_\Gamma)}{\partial \mathbf{n}'_\Gamma} d\Gamma' \cong \sum_{j=1}^{I} \left\{ \left[\frac{\partial \hat{q}_{g'}}{\partial \mathbf{n}_\Gamma}\right]_j \frac{d_j}{2} \int_{-1}^{1} \tilde{\psi}_h\left[\mathbf{r}_{\Gamma,i}, \mathbf{r}_{\Gamma_j}(\tau)\right] d\tau \right\} \end{cases} \tag{1.15}$$

The integrals herewith appearing involves the fundamental solutions of the *Green's* function. Owing to no explicit expression available, they are obtained by application of a numerical integration formula, namely:

$$\int_{-1}^{1} f(\tau) d\tau \simeq \sum_{k=1}^{K} \omega_k f(\tau_k), \tag{1.16}$$

where ω_k and τ_k are the quadrature weights and abscissas, respectively. A standard *Gauss-Legendre* formula is used in the work.

At last, the problem is cast into the following algebraic matrix-response form:

$$\sum_{g'=1}^{G} \sum_{j=1}^{I} M_{ij}^{gg'} J_{g',j}^{+} = \sum_{g'=1}^{G} \sum_{j=1}^{I} \left\{ N_{ij}^{gg'} J_{g',j}^{-} + O_{ij}^{gg'} q_{g',j} + P_{ij}^{gg'} \left(\frac{\partial q_{g'}}{\partial \mathbf{n}_\Gamma}\right)_j + Q_{ij}^{gg'} \hat{q}_{g',j} + R_{ij}^{gg'} \left(\frac{\partial \hat{q}_{g'}}{\partial \mathbf{n}_\Gamma}\right)_j \right\}, \qquad i = 1, 2, \ldots, I, \quad g = 1, 2, \ldots, G, \tag{1.17}$$

where

$$
\begin{aligned}
M_{ij}^{gg'} &= \frac{c(\mathbf{r})}{2}\delta_{ij}\delta_{gg'} + \frac{d_j}{2}\int_{-1}^{1} \tilde{J}_{gg'}^{-}\left[\mathbf{r}_{\Gamma,i}, \mathbf{r}_{\Gamma_j}(\tau)\right] d\tau, \\
N_{ij}^{gg'} &= -\frac{c(\mathbf{r})}{2}\delta_{ij}\delta_{gg'} + \frac{d_j}{2}\int_{-1}^{1} \tilde{J}_{gg'}^{+}\left[\mathbf{r}_{\Gamma,i}, \mathbf{r}_{\Gamma_j}(\tau)\right] d\tau, \\
O_{ij}^{gg'} &= -\sum_{h=1}^{G}\frac{\sigma_{gh}\sigma_{hg'}^{*}}{4B_h^2}\left\{c(\mathbf{r})\delta_{ij} + \frac{d_j}{2}\int_{-1}^{1}\frac{\partial\tilde{\psi}_h}{\partial\mathbf{n}'_\Gamma}\left[\mathbf{r}_{\Gamma,i}, \mathbf{r}_{\Gamma_j}(\tau)\right] d\tau\right\}, \\
P_{ij}^{gg'} &= \sum_{h=1}^{G}\frac{\sigma_{gh}\sigma_{hg'}^{*}}{4B_h^2}\frac{d_j}{2}\int_{-1}^{1}\tilde{\psi}_h\left[\mathbf{r}_{\Gamma,i}, \mathbf{r}_{\Gamma_j}(\tau)\right] d\tau, \\
Q_{ij}^{gg'} &= \sum_{h=1}^{G}\frac{\sigma_{gh}\sigma_{hg'}^{*}}{4B_h^4}\left\{c(\mathbf{r})\delta_{ij} + \frac{d_j}{2}\int_{-1}^{1}\frac{\partial\tilde{\psi}_h}{\partial\mathbf{n}'_\Gamma}\left[\mathbf{r}_{\Gamma,i}, \mathbf{r}_{\Gamma_j}(\tau)\right] d\tau\right\}, \\
R_{ij}^{gg'} &= -\sum_{h=1}^{G}\frac{\sigma_{gh}\sigma_{hg'}^{*}}{4B_h^4}\frac{d_j}{2}\int_{-1}^{1}\tilde{\psi}_h\left[\mathbf{r}_{\Gamma,i}, \mathbf{r}_{\Gamma_j}(\tau)\right] d\tau.
\end{aligned}
\tag{1.18}
$$

1.2.3 The problem of the volume source distribution in rectangular domain

The reduction of the source volume integral gives us an approach to implement the BEM algorithm. However, one has to collect some information to build up the approximated spatial distribution. Actually, pointwise partial currents on boundary elements are known from the latest power outer iteration. By using the relationship between currents and fluxes, one can immediately generate the fission source for the next neutron fission generation. Therefore, fitting to the fission source distribution by generated pointwise source is a way to approximate the distribution which is necessary for Equation (1.12) or (1.13). In this work, the domain of the core is subdivided into a number of rectangular nodes in a 2D Cartesian coordinate system. In addition, it is necessary to construct a formula for the source term, as well as the boundary integrals, under the application of the zero-th, first, second and third-order approximations, in order to investigate the different corresponding behaviors. Thus, the derivation of the fitting of the source volume distribution for four approximations is outlined in this section.

Zero-th order

The zero-order fitting $q_g(x, y)$ in the 2D (x,y) node n can be easily constructed as:

$$q_g(x, y) \simeq \bar{q}_g,$$

where $\bar{q}_g$, obviously, is the average neutron source in the domain $x \in \left[-\frac{A}{2}, \frac{A}{2}\right], y \in \left[-\frac{B}{2}, \frac{B}{2}\right]$. It may be determined by the neutron conservation equation over the domain. Then, we have:

$$q_{g,i} = \bar{q}_g, \qquad \left[\frac{\partial q_g}{\partial x_\Gamma}\right]_i = \left[\frac{\partial q_g}{\partial y_\Gamma}\right]_i = 0. \tag{1.19}$$

First order

For first-order approximations $q_g(x, y)$ is defined as a linear function:

$$q_g(x, y) = l_{0,0} + l_{1,0}x + l_{0,1}y. \tag{1.20}$$

Thus, we have:

$$q_{g,i} = l_{0,0} + l_{1,0}x_i + l_{0,1}y_i, \qquad \left[\frac{\partial q_g}{\partial x_\Gamma}\right]_i = l_{1,0}, \qquad \left[\frac{\partial q_g}{\partial y_\Gamma}\right]_i = l_{0,1}. \tag{1.21}$$

To determine $l_{0,0}$, $l_{1,0}$ and $l_{0,1}$, by firstly integrating $q_g(x, y)$ over the domain and dividing by the domain area, we have:

$$\frac{1}{AB}\int_{-\frac{B}{2}}^{\frac{B}{2}}\int_{-\frac{A}{2}}^{\frac{A}{2}} q_g(x,y)dxdy = \frac{1}{AB}\int_{-\frac{B}{2}}^{\frac{B}{2}}\int_{-\frac{A}{2}}^{\frac{A}{2}} \left(l_{0,0} + l_{1,0}x + l_{0,1}y\right)dxdy = l_{0,0}. \tag{1.22}$$

The average neutron source $\bar{q}_g$ is defined as above. Thus, the coefficient $l_{0,0}$ may be eliminated from Equation (1.21) as:

$$q_g(x, y) = l_{1,0}x + l_{0,1}y + \bar{q}_g. \tag{1.23}$$

Consequently, $l_{1,0}$ and $l_{0,1}$ can be evaluated by using a standard *least-square* fitting approach. The problem can be nicely written in a matrix form:

$$\mathbf{Ml} = \mathbf{k}, \tag{1.24}$$

where

$$\mathbf{M} = \begin{bmatrix} x_1 & y_1 \\ x_2 & y_2 \\ \vdots & \vdots \\ x_N & y_N \end{bmatrix}, \quad \mathbf{l} = \begin{bmatrix} l_{1,0} \\ l_{0,1} \end{bmatrix}, \quad \mathbf{k} = \begin{bmatrix} q_{g,1} - \bar{q_g} \\ q_{g,2} - \bar{q_g} \\ \vdots \\ q_{g,N} - \bar{q_g} \end{bmatrix}. \tag{1.25}$$

The coordinates (x_n, y_n) identify the N locations at which the source takes the value of $q_{g,n}$. By left multiplication of Equation (1.24) by $\mathbf{M}^T$, the normal equations are obtained for the problem, as:

$$\mathbf{l} = (\mathbf{M}^T\mathbf{M})^{-1}\mathbf{M}^T\mathbf{k} = \mathbf{Gk},$$

The system of equations above yields the value of $l_{1,0}$ and $l_{0,1}$. Actually, the I middle points $\mathbf{r}_{\Gamma,i}$ of the boundary elements on the boundary are selected.

Second and third order

For the second-order and the third-order fitting approach, the derivation follows in the same way. We increase the order as:

$$q_g(x, y) = l_{0,0} + l_{1,0}x + l_{0,1}y + l_{2,0}x^2 + l_{1,1}xy + l_{0,2}y^2. \tag{1.26}$$

for the second order, and

$$\begin{aligned} q_g(x, y) = l_{0,0} + l_{1,0}x + l_{0,1}y + l_{2,0}x^2 + l_{1,1}xy + l_{0,2}y^2 + l_{3,0}x^3 \\ + l_{2,1}x^2y + l_{1,2}xy^2 + l_{0,3}y^3. \end{aligned} \tag{1.27}$$

for the third order. Correspondingly, the changes of parameters related to the boundary integrals, as compared with those in formula (1.21), are listed in Table (1.2), and the matrix $\mathbf{M}$ as well as the vector $\mathbf{l}$ are shown in Table (1.3).

Table 1.2: Formula of the source nodal distribution with different order polynomials

Order	$q_{g,i}$	$\left[\frac{\partial q_g}{\partial x_\Gamma}\right]_i$	$\left[\frac{\partial q_g}{\partial y_\Gamma}\right]_i$
0	$\bar{q}_g$	0	0
1	$l_{1,0}x_i + l_{0,1}y_i + \bar{q}_g$	$l_{1,0}$	$l_{0,1}$
2	$l_{1,0}x_i + l_{0,1}y_i + l_{2,0}x_i^2 + l_{1,1}x_iy_i + l_{0,2}y_i^2 + \bar{q}_g - l_{2,0}A^2/12 - l_{0,2}B^2/12$	$l_{1,0} + 2l_{2,0}x_i + l_{1,1}y_i$	$l_{0,1} + l_{1,1}x_i + 2l_{0,2}y_i$
3	$l_{1,0}x_i + l_{0,1}y_i + l_{2,0}x_i^2 + l_{1,1}x_iy_i + l_{0,2}y_i^2 + l_{3,0}x_i^3 + l_{2,1}x_i^2y_i + l_{1,2}x_iy_i^2 + l_{0,3}y_i^3 + \bar{q}_g - l_{2,0}A^2/12 - l_{0,2}B^2/12$	$l_{1,0}+2l_{2,0}x_i+l_{1,1}y_i+3l_{3,0}x_i^2+2l_{2,1}x_iy_i+l_{1,2}y_i^2$	$l_{0,1}+l_{1,1}x_i+2l_{0,2}y_i+l_{2,1}x_i^2+2l_{1,2}x_iy_i+3l_{0,3}y_i^2$
	$\hat{q}_g$	$\left[\frac{\partial \hat{q}_g}{\partial x_\Gamma}\right]_i$	$\left[\frac{\partial \hat{q}_g}{\partial y_\Gamma}\right]_i$
0	0	0	0
1	0	0	0
2	$2l_{2,0} + 2l_{0,2}$	0	0
3	$2l_{2,0}+2l_{0,2}+6l_{3,0}x_i+2l_{2,1}y_i+2l_{1,2}x_i+6l_{0,3}y_i$	$6l_{3,0} + 2l_{1,2}$	$2l_{2,1} + 6l_{0,3}$

Table 1.3: Column n of $\mathbf{M}$ and vector $\mathbf{l}$ with different orders

	Order	Size	
Column n of $\mathbf{M}$	1	2	$[x_n, y_n]$
	2	5	$[x_n, y_n, x_n^2 - A^2/12, x_ny_n, y_n^2 - B^2/12]$
	3	9	$[x_n, y_n, x_n^2 - A^2/12, x_ny_n, y_n^2 - B^2/12, x_n^3, x_n^2y_n, x_ny_n^2, y_n^3]$
	Order	Size	
Vector $\mathbf{l}$	1	2	$[l_{1,0}, l_{0,1}]^T$
	2	5	$[l_{1,0}, l_{0,1}, l_{2,0}, l_{1,1}, l_{0,2}]^T$
	3	9	$[l_{1,0}, l_{0,1}, l_{2,0}, l_{1,1}, l_{0,2}, l_{3,0}, l_{2,1}, l_{1,2}, l_{0,3}]^T$

When the second and the third order polynomials are applied, the problem becomes more complicated. As well known as *Runge's* phenomenon, higher order polynomials lead to the instability of the iterated procedure, because they can be highly oscillatory. Thus, the non-convergence is investigated based on the variety of calculated examples. Higher order polynomials also allow us to introduce the coordinate cross terms. They may play a role on the precision of the fitting. The influence from this factor is explored as well.

1.2.4 Full core calculation

For the full core calculation, the system is subdivided into sub regions, numbered by $n = 1, 2, \ldots, N$. These regions are considered as nodes on which BEM will be based and a response matrix for each of them is constructed. As well known, full core calculation is divided into two level of iterations, spatial inner iteration and power outer iteration. In the sections above, the numerical solution of BEM in one node is described. This procedure can be embedded into the global iteration for full core calculation. The procedure, for instance for the third-order source approximation model, is described in algorithm (1).

Algorithm 1 Global iteration

calculate: $\mathbf{N}, \mathbf{O}, \mathbf{P}, \mathbf{Q}, \mathbf{R}, \mathbf{G}$
$i \leftarrow 0$
initialize: k_i, ϕ_i
repeat
  $i \leftarrow i + 1$
  refresh: $\mathbf{q}_i, \bar{\mathbf{q}}_i, \mathbf{l}_i, \frac{\partial \mathbf{q}_i}{\partial x_\Gamma}, \frac{\partial \mathbf{q}_i}{\partial y_\Gamma}, \hat{\mathbf{q}}_i, \frac{\partial \hat{\mathbf{q}}_i}{\partial x_\Gamma}, \frac{\partial \hat{\mathbf{q}}_i}{\partial y_\Gamma}$
  repeat
    calculate: $\mathbf{J}^+$
    calculate: ϕ
  until error$(\phi) \leq \epsilon_{in}$
  $refresh : \mathbf{J}_i^+, \phi_i$
  calculate: k_i
until error$(k_i) \leq \epsilon_{out}$

At the beginning, the response matrix elements are prepared before the iteration process starts up, as well as the matrix, $\mathbf{G}$, for least-square fitting. At the same time, initial guesses of fluxes and multiplication constant are generated. Then, the power outer iteration begins with the neutron source distribution approximation for each node. Given by source term, spatial inner iteration is used to compute outgoing currents $\mathbf{J}^+{}_i$ as well as the fluxes. It continues till the converged criterion, ϵ_{in}, is satisfied by judging the error of fluxes of each nodes between two successive iteration steps. New fluxes and multiplication constant are obtained for the next loop of power outer iteration. The entire iteration is terminated by checking the relative difference between k_i and k_{i-1} to satisfy another converged criterion ϵ_{out}.

1.3 Evaluation of the Gauss-Legendre quadrature approach for the integration of function $K_0(x)$

In the BEM algorithm, integrals of modified Bessel functions of second kind (zero order), $K_0(x)$, is impossible to be given an analytical solution. Gauss-Legendre Quadrature (GLQ) approach is applied for practical calculations. Errors always exist when the GLQ approach is applied for calculating integrals of $K_0(x)$. On the other hand, the error may be also caused by round-off errors of computers. In this section, the contributions to error are estimated by practical computations, in order to give conclusions on how and to what extent the errors will impact on the BEM algorithm.

1.3.1 GLQ approach on integral of $K_0(x)$

The problem to be solved is normally the integration of $K_0(x)$ over domain $[a, b]$. Below the expression of modified Bessel function of second kind, K_α, is given:

$$K_\alpha(x) = \frac{\pi}{2} \frac{I_{-\alpha}(x) - I_\alpha(x)}{\sin(\alpha\pi)} = \frac{\pi}{2} i^{\alpha+1} H_\alpha^{(1)}(ix). \tag{1.28}$$

In particular,

$$K_0(x) \approx \begin{cases} -\ln \dfrac{x}{2} - \gamma & \text{if } 0 < x \ll 1, \\ \sqrt{\dfrac{\pi}{2x}} e^{-x} & \text{if } x \gg \dfrac{1}{4}. \end{cases} \tag{1.29}$$

K_0 is regular if $[a, b]$ does not approach the origin. In particular, it is singular at $x = 0$ so that the integral over $(0, b]$ has to be carefully studied, to establish if the GLQ approach can be applied properly

for the integration of the singular function. For convenience, we only take the first formula which is for $0 < x \ll 1$ in Equation (1.29) to evaluate the integration because only this formula contains the singular term $\ln \frac{x}{2}$. It appears that $\ln \frac{x}{2}$ is a log-type function, so that the integral over $(0, b]$ must be convergent. Also, using the function expansion, one can write:

$$\begin{aligned} K_0(x) &= -\left(\gamma + \ln \frac{x}{2}\right) I_0(x) + \frac{x^2}{4} + \frac{3x^4}{128} + \cdots \\ &= -\ln \frac{x}{2} - \gamma - (\gamma + \ln \frac{x}{2})(I_0(x) - 1) + (\frac{x^2}{4} + \frac{3x^4}{128} + \cdots) \end{aligned} \tag{1.30}$$

only if the argument x is a sufficiently small value. It can be proved that $K_0(x)$ is the sum of a singular part and a regular part by the following derivations:

$$\begin{aligned} \lim_{x\to 0} \left(\gamma + \ln \frac{x}{2}\right)(I_0(x) - 1) &= \lim_{x\to 0} \left(\gamma + \ln \frac{x}{2}\right)\left(\frac{x^2}{4} + \frac{x^4}{64} + \frac{x^6}{2304} + \cdots\right) \\ &\le \lim_{x\to 0} \left(\gamma + \ln \frac{x}{2}\right)\left(\frac{x^2 + x^4 + x^6 + \cdots}{4}\right) \\ &= \lim_{x\to 0} \frac{\gamma + \ln \frac{x}{2}}{\frac{4}{x^2} - 4} = 0 \end{aligned}$$

and

$$\begin{aligned} \lim_{x\to 0} \left(\frac{x^2}{4} + \frac{3x^4}{128} + \cdots\right) &\le \lim_{x\to 0} \frac{1}{4}\left(x^2 + x^4 + x^6 + \cdots\right) \\ &= \lim_{x\to 0} \frac{x^2}{4(1 - x^2)} = 0. \end{aligned}$$

Then, observing the special expression of $K_0(x)$ with a singular term and a regular term

$$K_0(x) = \underbrace{-\ln \frac{x}{2} - \gamma}_{\text{singular}} + \underbrace{K_0(x) + \ln \frac{x}{2} + \gamma}_{\text{regular}}, \tag{1.31}$$

we are able to perform the integration of $K_0(x)$ through evaluating the integral of the singular term analytically and calculating the integral of the regular term by GLQ approach. The singular part is integrated as:

$$\int_0^b -\ln \frac{x}{2} - \gamma dx = \left(-x \ln \frac{x}{2} - \gamma x + x\right)\Big|_0^b = b\left(-\ln \frac{b}{2} + 1 - \gamma\right). \tag{1.32}$$

In fact, the regular term $K_0(x) + \ln \frac{x}{2} + \gamma$ converges to zero when $x \to 0$ which implies the regular term is the difference of two singular terms, $K_0(x)$ and $-\ln \frac{x}{2} - \gamma$. Noted that in order to avoid round-off errors from computers due to the subtraction of two large numerical values from two singular terms, $-\ln \frac{x}{2} - \gamma$ is selected to be the analytical term instead of $-\ln \frac{x}{2}$.

1.3.2 Full numerical GLQ and semi-analytical GLQ approaches

Table (1.4) shows the values of $K_0(x)$, $-\ln \frac{x}{2} - \gamma$ and their differences over a large range, $[10^{-50}, 10^{50}]$. At first, it seems to grow slowly when x approaches the origin. Therefore, it is not affirmative that

Table 1.4: $K_0(x)$, $-\ln\frac{x}{2}$ and their difference

x	$K_0(x)$	$-\ln\frac{x}{2}-\gamma$	Difference
10^{-50}	115.245	115.245	0.000
10^{-20}	46.168	46.168	0.000
10^{-10}	23.142	23.142	0.000
10^{-5}	11.629	11.629	$3.158 \cdot 10^{-10}$
10^{-2}	4.721	4.721	$1.430 \cdot 10^{-4}$
10^{-1}	2.427	2.419	$8.552 \cdot 10^{-3}$
1	0.421	0.116	0.3051
10^{1}	$1.778 \cdot 10^{-5}$	−2.187	2.187
10^{2}	$4.657 \cdot 10^{-45}$	−4.489	4.489
10^{5}	0.000	−11.397	11.400
10^{10}	0.000	−22.910	22.910
10^{50}	0.000	−115.013	115.000

evaluating integrals by directly using GLQ will give enough accuracy. Secondly, the difference grows up when x increases from 1 to much larger values. For both reasons, two approaches, which are Full-Numerical GLQ (FNQ) and Semi-Analytical GLQ (SAQ), are evaluated and compared with each other. FNQ approach is given by the formula

$$\int_0^b K_0(x)dx = \sum_{p=1}^{P} \omega_p K_0(x_p), \tag{1.33}$$

and SAQ approach reduces to the formula

$$\int_0^b K_0(x)dx = b\left(-\ln\frac{b}{2}+1-\gamma\right) + \sum_{p=1}^{P} \omega_p \left[K_0(x_p)+\ln\frac{x_p}{2}+\gamma\right]. \tag{1.34}$$

In three cases, integrations with different numbers of abscissas (called by A_n) over three different domains, $(0, 0.001]$, $(0, 1]$ and $(0, 1000]$, are calculated, as can be seen in Figure (1.2,1.3 and 1.4). At last, with the purpose of comparison, the integral of $-\ln\frac{x}{2}-\gamma$ is also calculated, since it is almost equivalent to $K_0(x)$ when x is less than 1 and there an analytical solution is possible.

Firstly, the integral of $K_0(x)$ over $(0, 0.001]$ is calculated by FNQ and SAQ, and the integral of $-\ln\frac{x}{2}-\gamma$ by FNQ. As shown in Figure (1.2), the value of the integral of $-\ln\frac{x}{2}-\gamma$ given by FNQ is quite precise when the number of abscissas increases. So, it implies that FNQ is applicable for integration of such log- type singular function in (0,0.001]. In addition, the value of the integral of $K_0(x)$ and $-\ln\frac{x}{2}-\gamma$ are quite close in the domain. Therefore, one can say FNQ is applicable for the integration of K_0 as well. Compared with the results on the integration of $-\ln\frac{x}{2}-\gamma$ by SAQ, it gives the same amount of error. Note that the reference value for K_0 is from the value by SAQ with A_{2048} because the integrals by SAQ converge rapidly when the number of abscissas increases in this case. Therefore, SAQ is superior to FNQ at least when b is small.

Secondly, the same integrals as in the first case are calculated by just changing the domain to $(0, 1]$. Figure (1.3) shows FNQ still gives the same level of estimation on $-\ln\frac{x}{2}-\gamma$, as well as on $K_0(x)$, as compared with the first case. However, SAQ illustrates lower precision and worse convergence than in the first case. The reason is that larger differences appear when x become large, as can be seen in Table (1.4).

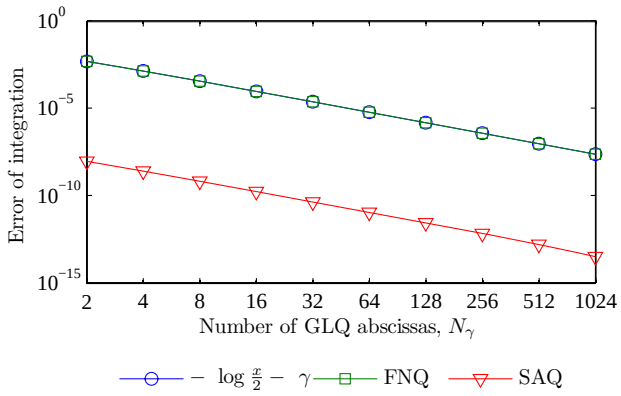

Figure 1.2: Error of integration over $(0, 0.001]$

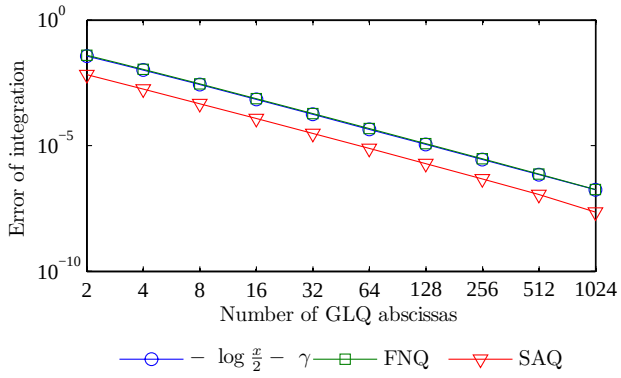

Figure 1.3: Error of integration over $(0, 1]$

At last, the right limit of the domain, b, becomes even larger, up to to 1000, in the third case. From Figure (1.4), the integration of $-\ln\frac{x}{2}-\gamma$ over $(0, 1000]$ by FNQ keeps the convergence and precision as above. On the contrary, precision of the integral of $K_0(x)$ by both FNQ and SAQ deteriorates. SAQ shows even worse convergence and precision than FNQ. The inaccuracy is even larger in the third case. It implies that SAQ will be less suitable for the integration of K_0 when the domain becomes large. The reference value is also given by the average of the integrals by FNQ and SAQ with A_{2048}.

1.3.3 Error from the FNQ approach over various integration domains

Clearly, increasing the number of abscissas will improve the accuracy of integration over the same domain. However, we may also be interested in the integration over different domains with the same number of abscissas because the domain over which integration is carried out changes when the global iteration is performed with various number of nodes. The increase of the number of nodes, with a corresponding reduction of the nodal size, will not only cause a higher accuracy from the perspective of refining the meshes but also will lead to higher accuracy of the integral of $K_0(x)$, therefore improving the precision of the response matrix as a by-product. At a first glance, it should be reasonable that the integration by FNQ or SAQ will be more precise with a small node size. However, in some results of practical calculations, such characteristics cannot be seen clearly. Therefore, it is necessary to evaluate

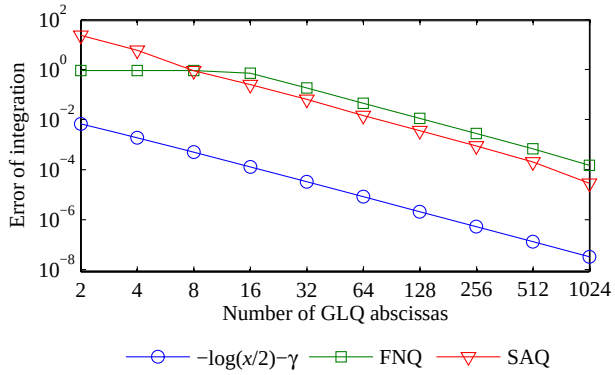

Figure 1.4: Error of integration over $(0, 1000]$

the feature on such issue.

Based on this thought, the integrals of $K_0(x)$ over different domains are tested by DA approach. Figure (1.5) shows the errors on integrals of $K_0(x)$ over $(0, b]$ versus the right end of the domain, b, by FNQ approach with A_4, A_{32}, A_{256}, A_{2048}. Curves indicate that the error of the integral evaluation decreases by a rather low rate, while b decreases. For instance, the error with A_{256} decreases from about the level of 10^{-5} to 10^{-6} while b decreases from 1 to 10^{-5}. In addition, the curves of the error illustrate nearly linear decreases. Unfortunately, by a simple refinement of the nodal size, it is hard to reduce the error, while increasing the number of FNQ abscissas is rather efficient.

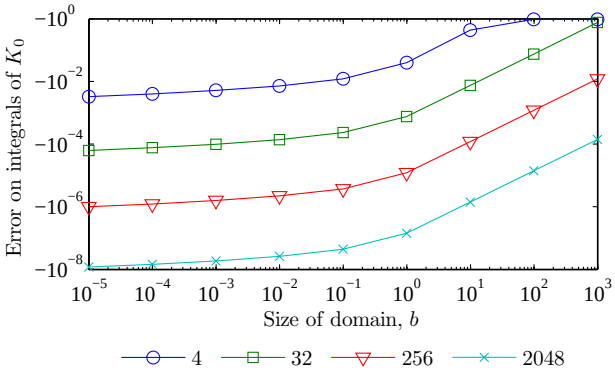

Figure 1.5: Error on integrals of $K_0(x)$ over $(0, b]$

Let us go back to the final BEM matrix-response equations. For convenience, we write the model as

$$\mathbf{M}\mathbf{J}^{+} = \mathbf{N}\mathbf{J}^{-} + \mathbf{O}\mathbf{q} \tag{1.35}$$

The physical significance of matrix $\mathbf{M}$, $\mathbf{N}$ and $\mathbf{O}$ is connected to the neutronic response of the physical and geometrical characteristics for the corresponding node. That is why it is called response-matrix. Therefore, only the physical and geometrical information is included in the matrix. From the

Boundary Elements approach, they are formulated as:

$$M_{ij}^{gg'} = \frac{c(\mathbf{r})}{2}\delta_{ij}\delta_{gg'} + \frac{d_j}{2}\int_{-1}^{1} \tilde{J}_{gg'}^{-}\left[\mathbf{r}_{\Gamma,i}, \mathbf{r}_{\Gamma_j}(\tau)\right] d\tau. \tag{1.36}$$

Ideally, there would not be any approximation if the integral on the RHS in Formula (1.36) is carried out exactly. It that case it would truly account for the response to the physical and geometrical characteristics. However, it is calculated practically by the FNQ approach introduced above and therefore some error is generated. This error can be considered as a distortion of the physical and geometrical characteristics, as the diffusion property, absorption or fission, of the corresponding node. It will lead to the shift of neutron diffusion behavior such as the variation of flux, current and finally the multiplication factor, k. Therefore, this shift is entirely different from the error caused by the numerical discretization from like Finite-Difference and Coarse-Mesh approaches. In other words, the error is inside the kernel of each node and it is hard to be reduced simply by refining the size of the nodes.

According to such interpretation, in the results for practical calculations by BEM, this may justify why k is not converging to the analytical reference value when the number of nodes increases.

1.3.4 Summary and conclusions

High accuracy of the FNQ approach on the integration of $-\ln\frac{x}{2} - \gamma$ proves that FNQ is suitable for estimating the integrals of log type singular functions over $(0, b]$. By comparison of FNQ and SAQ approaches, the latter is more efficient when the right limit of the domain, b, is small enough. The convergence and precision of both approaches are similar when b becomes larger. Results do not show any computational instability to worry about when the difference of $K_0(x)$ and $-\ln\frac{x}{2} - \gamma$ is numerically calculated by computers.

Errors on the integration of $K_0(x)$ by the FNQ approach are studied with different sizes of the domain. Results show a low rate of reduction which implies that increasing the number of nodes and therefore decreasing their size is not an efficient way to cut the FNQ-caused error.

1.4 Numerical results on homogeneous model

Two homogeneous models, a 1D single group diffusion with external plane source and a 2D three groups critical problem, were calculated in order to verify the performance of the BEM approach. Their analytical solutions are easy to be obtained so that they can be considered as benchmarks. Moreover, the comparison with other numerical approaches is also important in order to evaluate the features of the BEM applied to neutron diffusion problems, so corresponding results from Finite-different (FD) and Nodal method (NM) approaches are introduced. The identification of the different schemes and parameters is given in Table (2.1).

1.4.1 1D one-group homogeneous model with external plane source

The purpose of the first model is to assess the BEM approach under the variation of the number of GLQ within each element, the number of elements within each node and the number of nodes along the x- and y-axis. Due to the absence of the fission source, there is no need for a volume source approximation.

The system analysed is shown in Figure (1.6): a finite rectangular ($a_{ex} = 10$cm and $h = 10$cm) homogeneous medium (one group constants: $D = 0.16$cm and $\Sigma_a = 0.02\text{cm}^{-1}$) with an external inward current (surface source), $J_{in}^{+} = 1$ neutron per cm^2 per second, located at $x = 0$. The boundary

Table 1.5: Identification on different schemes and parameters

ID	Denotation
FD	Finite-difference approach
NM	Nodal method approach
BEM_n	Boundary element method approach with nth-order source approximation
N_α	N nodes along each dimension
N_β	N boundary elements used for the discretization of each edge in a node
N_γ	N GLQ abscissas

conditions are zero current at $y = 0$ and $y = h$, and zero flux at $x = a_{ex}$. So, it can be considered as a fully 1D problem along the x-axis.

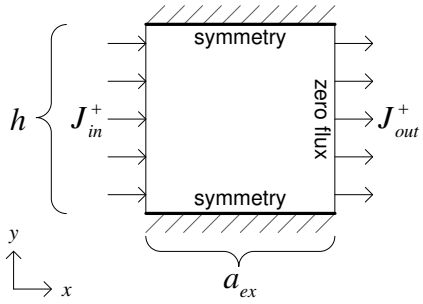

Figure 1.6: Configuration of 1D one group homogeneous model

The analytical solution for flux can be written as

$$\phi(x) = \frac{2J^+_{in}(0)\sinh\frac{a_{ex}-x}{L}}{\sinh\frac{a_{ex}}{L}+\cosh\frac{a_{ex}}{L}} \tag{1.37}$$

and the left edge outgoing partial current at $x = a_{ex}$ is

$$J^+_{out} = \frac{DJ^+(0)}{L\left(\sinh\frac{a_{ex}}{L}+\cosh\frac{a_{ex}}{L}\right)} = 5.9281262\cdot 10^{-3}, \tag{1.38}$$

where $L = \sqrt{D/\Sigma_a}$ is the diffusion length. Then, the outgoing current J^+_{out} is the main quantity investigated in this section.

N_γ is the basic factor dominating the accuracy of the boundary integrals. Thus, by increasing N_γ, a lower error on J^+_{out} is obtained, as seen in Figure (2.1), although the efficiency decreases when N_γ takes on very high values.

The influence of N_β on the accuracy of J^+_{out} can be seen in Figure (2.2). The decreasing rate of error is almost constant throughout the full range of values. The fact that the curves from different values of N_γ are very close implies that N_γ is less important for the accuracy of J^+_{out}. Furthermore, observing the profile of the outgoing current on the right surface in Figure (1.9), we realize that the error is caused by the inaccurate values at the elements close to the corners connecting to the other two surfaces. Such phenomena occur because the sharp angle of the corners do not allow to satisfy the requirement of smooth surface needed for the BEM. Besides, constant approximation of currents on boundary elements also does not take this fact into account sufficiently.

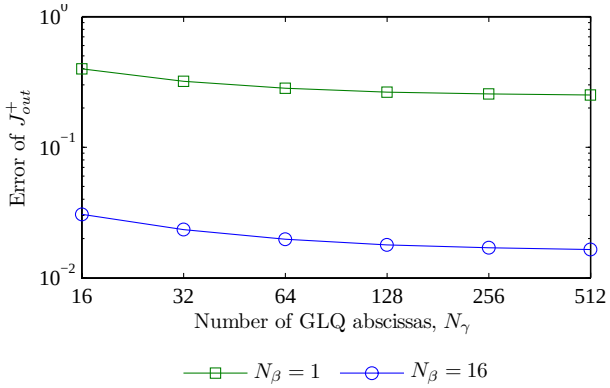

Figure 1.7: Outgoing current versus number of GLQ abscissas.

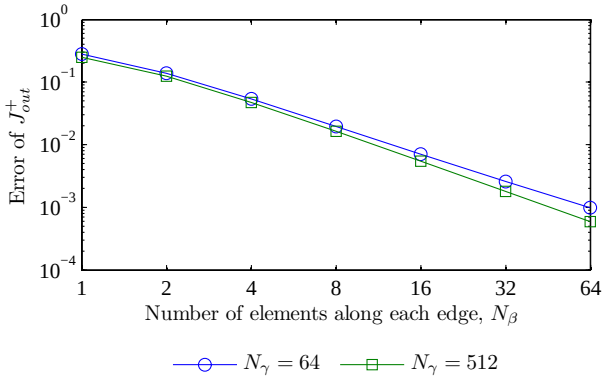

Figure 1.8: Error of outgoing current versus number of meshes in each element

All the cases above are performed just for a single node. Although it is not necessary to refer to a multi-node problem for the calculation of homogeneous configurations without volume external source, it is still highly helpful to evaluate the impact of multi-nodes in the BEM algorithm because of the presence in this case of volume external sources. For this reason, we divide the rectangle into several nodes with the same size ($\Delta x = a_{ex}/N_\alpha$, $\Delta y = h/N_\alpha$). Figure (1.10) shows there is no significant contribution for the improvement of the accuracy, although the smaller size of the nodes leads to finer boundary elements with the benefit of a higher accuracy on the boundary integrals and on currents. Such benefit contributes slightly at the left part of the second curve from $N_\beta = 16$. Then, the error grows very slowly as N_α becomes higher for both curves. The reason is that multi-nodes introduce internal currents which contains approximation from the discretization. Thois explains why multi-nodes is not always necessary for homogeneous systems using BEM.

Above all, the conclusion from the results of 1D homogeneous diffusion model is that high values of N_γ and N_β are positive but high values of N_α is do not affect accuracy significantly.

1.4.2 2D multi-group homogeneous model

In order to verify the performance of the BEM approach, critical calculations for a homogeneous rectangular system with geometric dimensions $160 \times 140\text{cm}^2$, with a fast reactor neutron spectrum profile, as shown in Table (2.2), is now performed. It can be considered as a benchmark because

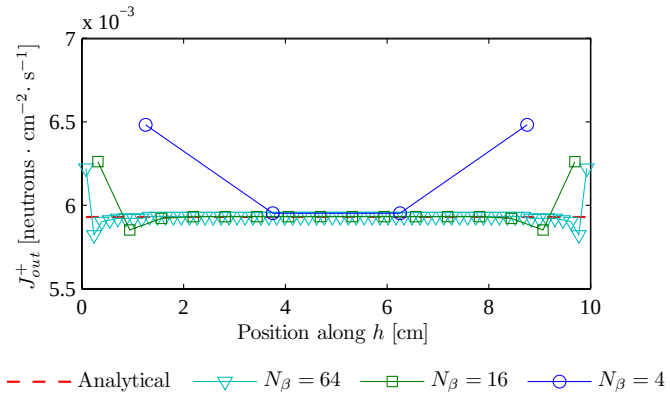

Figure 1.9: Profile of outgoing current along h

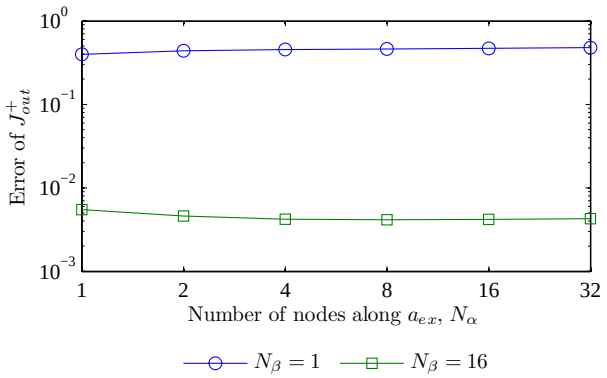

Figure 1.10: Error of outgoing current versus number of nodes along a_{ex}, $N_\gamma = 512$

the analytical solution is available. From another point of view, the comparison with other numerical approaches is also important to evaluate the features of the BEM applied for neutron diffusion problems, so that corresponding results from Finite-Difference (FD) and Nodal Method (NM) approaches are introduced as well. The calculation mainly illustrates the behavior of the multiplication factor k, under the variation of different approaches and parameters. The model is used to evaluate the BEM algorithm applied for critical calculations. These calculations introduce the fission source as a volume external source in the iteration process. Therefore, the importance of the approximation of the source term is evidenced.

Table 1.6: Material data for the homogeneous core

g	Σ_r^g $[10^{-2}\text{cm}^{-1}]$	$\nu\Sigma_f^g$ $[10^{-2}\text{cm}^{-1}]$	D^g [cm]	$\Sigma_s^{g\to 2}$ $[10^{-2}\text{cm}^{-1}]$	$\Sigma_s^{g\to 3}$ $[10^{-3}\text{cm}^{-1}]$	χ^g
1	3.0460	1.0760	2.11	2.5780	0.5164	0.7737
2	0.7060	0.3309	1.29	0.0000	4.7050	0.2193
3	0.6316	0.4366	0.86	0.0000	0.0000	0.0070

Effects from number of GLQ abscissas and boundary elements

Firstly, it is necessary to investigate what aspects influence the accuracy of the boundary integrals and then affect the response matrix which directly determines the accuracy of the applied BEM approach. Of course, N_α and N_β determine the size of each boundary element. However, apart from these factors, N_γ is the key factor which gives the accuracy of boundary element integrations and then the response matrix, as discussed above. For this reason, the effects of N_γ are investigated at the very beginning.

Figure (1.11) shows the variation of k and its error when N_γ changes from 16 to 512 in the case of $N_\alpha = 2$, $N_\beta = 4$. It is evident that k shows a converging behavior. However, it does not converge to the analytical value, k_{ana}, owing to the low value of $N_\alpha = 2$ and $N_\beta = 4$. The curves also show an asymptotic trend, which means that a lower value for N_γ leads to an overestimation of k.

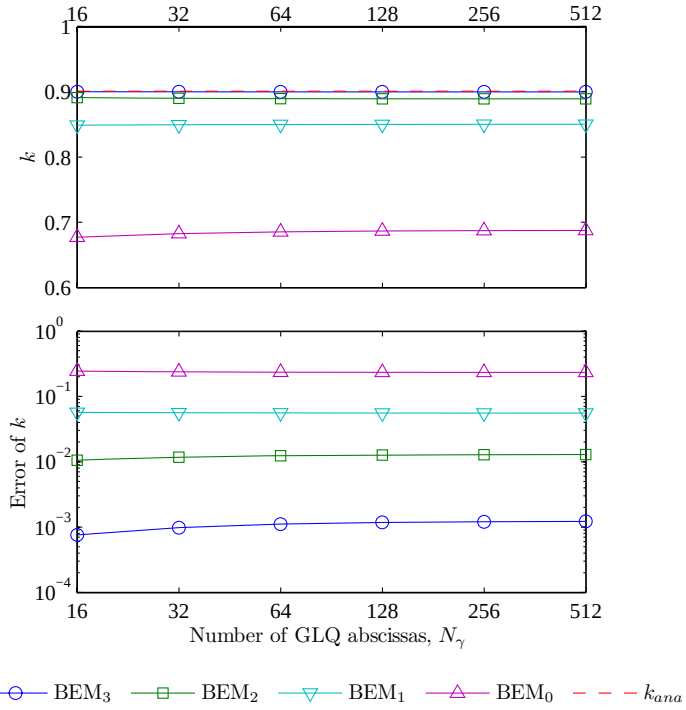

Figure 1.11: k and the error versus number of GLQ abscissas, $N_\alpha = 2$, $N_\beta = 4$

Secondly, given the size of a node, the size of each element is determined by N_β. This parameter affects partly the accuracy of the boundary integration because the same N_γ gives different accuracies over different sizes of the domain as shown in Section 1.3. However, if N_γ is quite large, such as 512, this influence can be ignored if other aspects are significant. Therefore, cases with different N_β under high value of N_γ might give have an effect of boundary discretization and constant approximation of partial currents on the boundary. Figure (1.12) shows k and its error versus N_β from 4 to 64 with the high value $N_\gamma = 512$. Curves simply converge to the asymptotes as well. The behavior is quite the same as that in Figure (1.11). Similarly, it implies that a lower N_β will give higher value of k.

Effects of the number of nodes

Theoretically, the BEM approach can converge to the analytical solution if there is no approximation on the volume integrals of the source term. However, the fission source in the algorithm is approximated

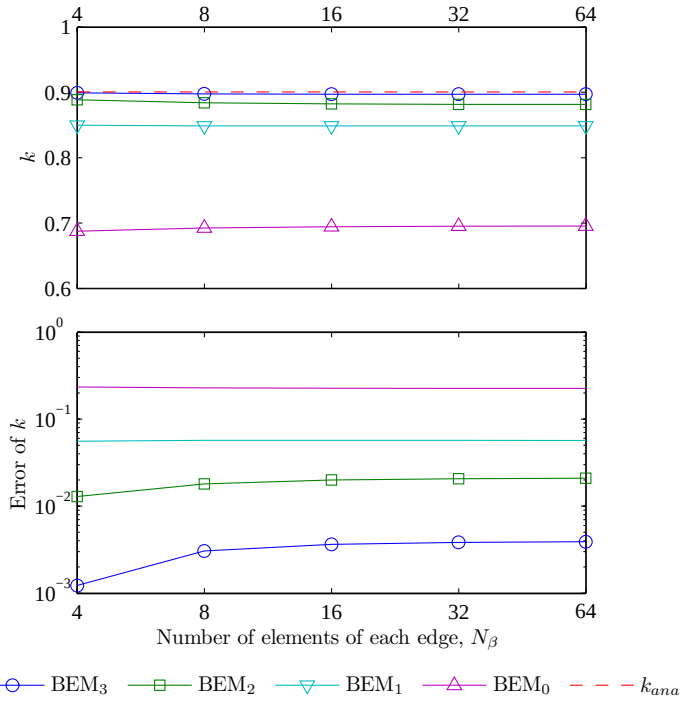

Figure 1.12: k and the error versus the number of meshes on each edge, $N_\alpha = 2$, $N_\gamma = 512$

as finite order polynomials. Thus, N_α affects the accuracy even if the boundary integrals are highly accurate. Different order approximations give various rates of convergence.

At first, we can ignore the inaccuracy from the two factors above when N_α is rather small and N_β and N_γ are quite large, because the error is dominated by the inaccuracy of the source term. As well known in nodal methods, k is underestimated, because a finite number of nodes normally leads to more leakage out of the boundary. This may explain the curves in Figure (1.12), as they converge to a value lower than the analytical solution, k_{ana}. The value can be considered as the analytical solution with a finite number of nodes.

By fixing $N_\beta = 32$ and $N_\gamma = 64$ and increasing N_α the critical calculation approaches k_{ana}, as seen in Table (1.7) and Figure (1.13). We also add the results from FD and NM approach for comparison.

Table 1.7: $k - k_{ana}$ with different N_α. $N_\beta = 32$, $N_\gamma = 64$

N_α	BEM_0	BEM_1	BEM_2	BEM_3	NM	FD
4	$-7.950\cdot10^{-02}$	$-4.487\cdot10^{-03}$	$-1.546\cdot10^{-03}$	$-6.648\cdot10^{-05}$	$-1.675\cdot10^{-04}$	$8.371\cdot10^{-03}$
8	$-2.248\cdot10^{-02}$	$-2.967\cdot10^{-04}$	$-6.165\cdot10^{-05}$	$-4.818\cdot10^{-06}$	$-1.077\cdot10^{-05}$	$2.119\cdot10^{-03}$
12	$-1.031\cdot10^{-02}$	$-4.322\cdot10^{-05}$	$1.991\cdot10^{-05}$	$-4.448\cdot10^{-06}$	$-2.148\cdot10^{-06}$	$9.271\cdot10^{-04}$
16	$-5.919\cdot10^{-03}$	$1.602\cdot10^{-06}$	$3.191\cdot10^{-05}$	$-4.628\cdot10^{-06}$	$-6.882\cdot10^{-07}$	$5.151\cdot10^{-04}$
20	$-3.862\cdot10^{-03}$	$1.450\cdot10^{-05}$	$3.436\cdot10^{-05}$	$-4.808\cdot10^{-06}$	$-2.982\cdot10^{-07}$	$3.265\cdot10^{-04}$
24	$-2.737\cdot10^{-03}$	$1.947\cdot10^{-05}$	$3.481\cdot10^{-05}$	$-4.988\cdot10^{-06}$	$-1.482\cdot10^{-07}$	$2.262\cdot10^{-04}$
28	$-2.057\cdot10^{-03}$	$2.182\cdot10^{-05}$	$3.477\cdot10^{-05}$	$-5.178\cdot10^{-06}$	$-8.818\cdot10^{-08}$	$1.626\cdot10^{-04}$
32	$-1.614\cdot10^{-03}$	$2.311\cdot10^{-05}$	$3.460\cdot10^{-05}$	—	$-5.818\cdot10^{-08}$	$1.209\cdot10^{-04}$
36	$-1.310\cdot10^{-03}$	$2.390\cdot10^{-05}$	$3.443\cdot10^{-05}$	—	$-4.817\cdot10^{-08}$	$9.234\cdot10^{-05}$
40	$-1.092\cdot10^{-03}$	$2.443\cdot10^{-05}$	$3.427\cdot10^{-05}$	—	$-3.818\cdot10^{-08}$	$7.187\cdot10^{-05}$

At first, FD, NM and BEM_0 show a monotonic behavior, while BEM_1, BEM_2 and BEM_3 have a

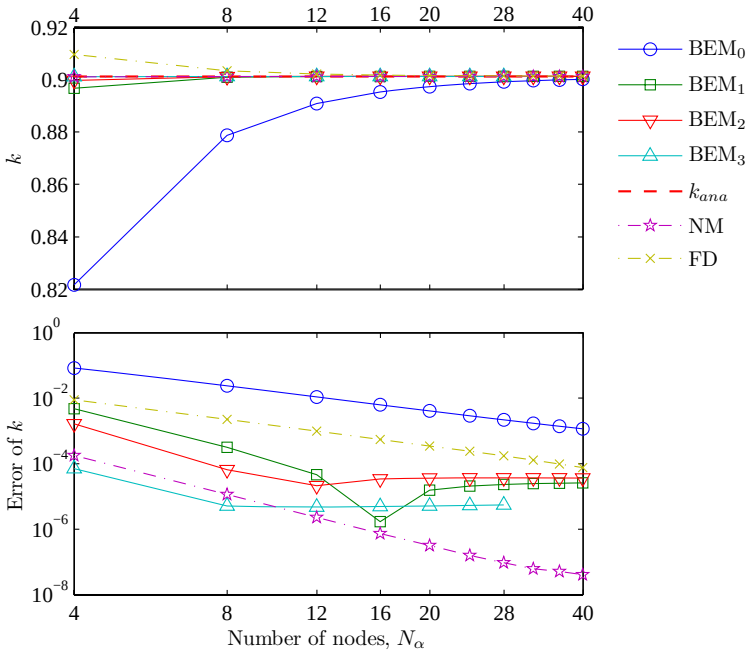

Figure 1.13: k and the error versus N_α. $N_\beta = 32$, $N_\gamma = 64$

non-linear behavior. Certainly, curves for FD and NM converge to the dashed line of k_{ana} when N_α becomes large. On the contrary, the relative errors of BEM_1, BEM_2 reach the degree of $E-5$ and $E-6$ for BEM_3. It is worth to notice that k of BEM_1 and BEM_2 goes across the dash line when N_α becomes large. It seems to converge to some asymptotes, instead of k_{ana}. The phenomenon is reasonable, because a large N_α significantly eliminates the error from the approximation on the source to a level lower than that associated to the factors, N_β and N_γ. The gaps between the asymptotes and k_{ana} can be considered as a BEM algorithm error. As analyzed in Section 1.3, the error partly from the BEM algorithm cannot vanish just by increasing N_α, so that gaps still exist when N_α becomes larger. The reason why the behavior does not appear on the curve of BEM_0 might be that the error caused by the approximation of volume source term is still too large to be ignored. In addition, k of BEM_3 remains under the dash line, differently from BEM_1 and BEM_2.

From the point of view of different order approximation for the volume source term, BEM_0 is the worst, even compared with FD. BEM_3 is the best at the rate of convergence at the beginning when N_α is larger than 12. BEM_2 performs even worse than BEM_2 when the curves reach saturation, although the former shows a higher rate of convergence.

Non-convergence behavior of BEM_3

As mentioned above, Runge's phenomenon might lead to the oscillation of higher ordered polynomials. It actually occurs when BEM_3 is used. Table (2.4) shows that k sometimes does not converge in the iteration procedure with different choices of N_α and N_β. A general conclusion is that the iteration process becomes non-convergent when N_α is larger than N_β.

Figure (1.14) shows the iteration procedure for k when it is non-converging. Larger differences between N_α and N_β lead to more serious disturbances, because large nodes with few boundary elements might give incorrect approximations of the volume source terms by Least-Square fitting, as seen in Figure (1.15). Comparing the case $N_\alpha = 8$ and $N_\beta = 16$ with the case $N_\alpha = 8$ and $N_\beta = 4$, it is

Table 1.8: k with different N_α for BEM_3. The figures underlined denote that the outer iterations are terminated at the 50-th cycle.

N_β	k				
	$N_\alpha = 2$	$N_\alpha = 4$	$N_\alpha = 8$	$N_\alpha = 16$	$N_\alpha = 32$
4	0.900559	0.901057	<u>1.337382</u>	<u>5.435735</u>	<u>21.128255</u>
8	0.898827	0.901364	0.901389	<u>1.895122</u>	<u>7.131109</u>
16	0.898219	0.901391	0.901438	0.901434	<u>2.788162</u>
32	0.898003	0.901389	0.901448	0.901448	0.901448
64	0.897926	0.901385	0.901452	0.901452	0.901452

possible to observe that high oscillations produce large negative values on the second group neutron source term in the node whose center is at $x = 61.25$cm,$y = 35$cm.

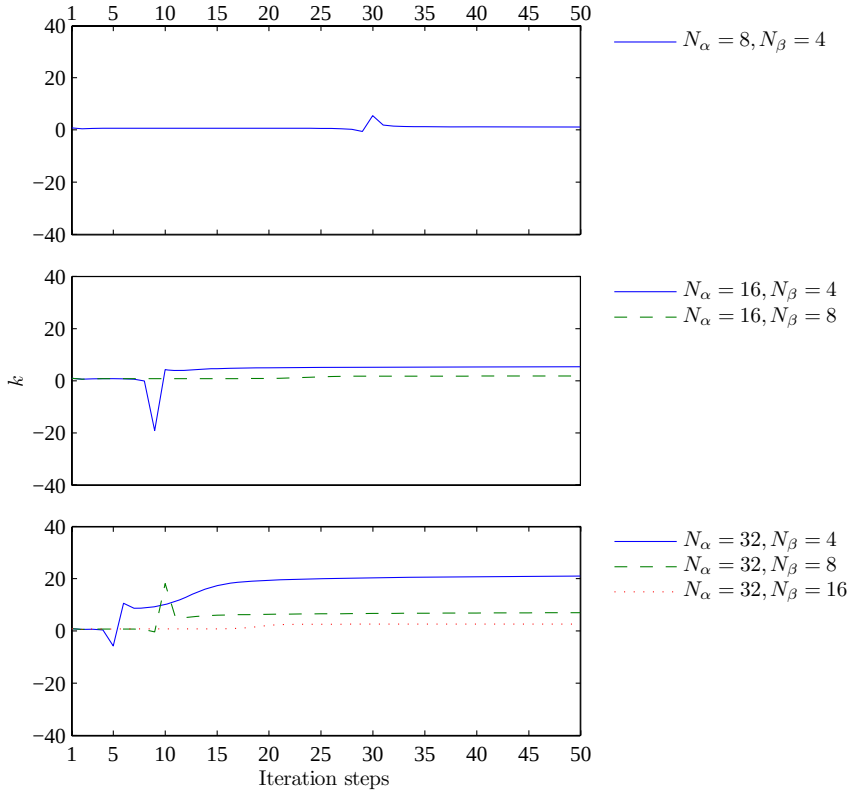

Figure 1.14: Non-convergence behavior of k in iterations. N_γ=64

CPU times

There are two contributions on the CPU time when a full core calculation is carried out. The first part is for the preparation of RM. It can be expressed by

$$T_{pre} \propto n_{mat} \cdot N_\beta^2 \cdot N_\gamma \tag{1.39}$$

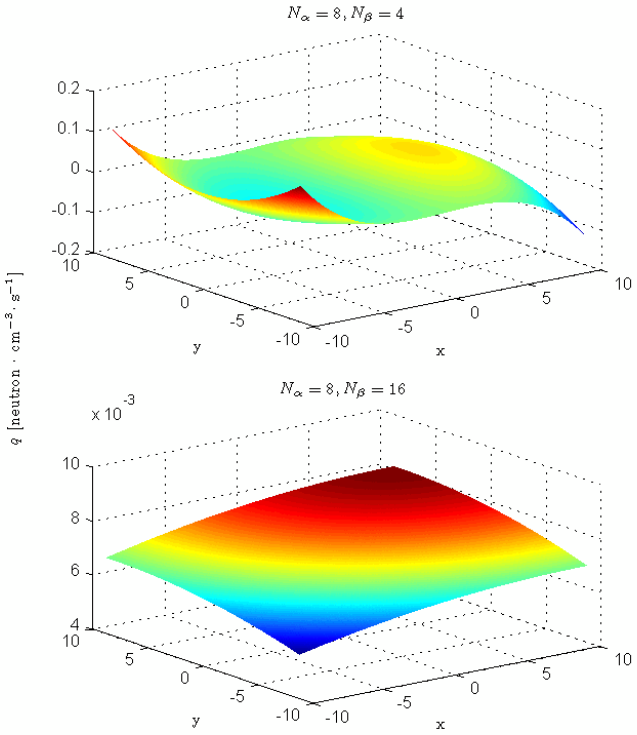

Figure 1.15: Least-Square fitting in the node whose center is at $x = 61.25$cm, $y = 35$cm. $N_\gamma = 64$

where n_{mat} denotes the number of materials. Formula (1.39) implies that the CPU time consumed by the preparation of RM is proportional to N_γ for integrations time: the dimension of the matrix times N_β^2 because N_γ decides the time for each integration, N_β^2 decides the dimension of matrix, and n_{mat} decides the total number of matrices. As shown in Figure (1.16), T_{pre} increases linearly when N_γ becomes larger with a fixed $N_\beta^2 = 8$ for BEM_3, so that Equation (1.39) is well proved. Actually, it is also satisfied by results from other BEM_n and different choices of N_α and N_β. On the other side, T_{pre} is also well proportional to N_β^2 when $N_\gamma = 16$ is fixed, as seen in Figure (1.17). However, large values of $N_\gamma = 16$ and N_β^2 lead to significant CPU times for the RM preparation. Non-homogeneous systems involve an increase of n_{mat} and, hence, time T_{pre}. At last, T_{pre} keeps constant if N_β^2 when N_γ are fixed even N_α^2 is changing in Figure (1.18), because the same size and material of nodes does not need any more calculations for RM.

The other part is for the iteration procedure. In particular, for critical calculations, the CPU time of the iteration procedure is

$$T_{it} \approx n_{cyc} \cdot t_c \tag{1.40}$$

where n_{cyc} and t_c denotes the total cycle number of inner iterations and CPU time consumed by each cycle of inner iteration, respectively. t_c can be written as

$$t_c \propto N_\alpha^2 \cdot N_\beta^2 \tag{1.41}$$

In practical cases, it is hard to evaluate n_{cyc}, because they are influenced by the initial guess of the multiplication constant, k, convergence criteria and acceleration methods. t_c is proportional to the number of RM related to N_α^2 times the square of dimension of RM related to N_β^2. The chart in Figure

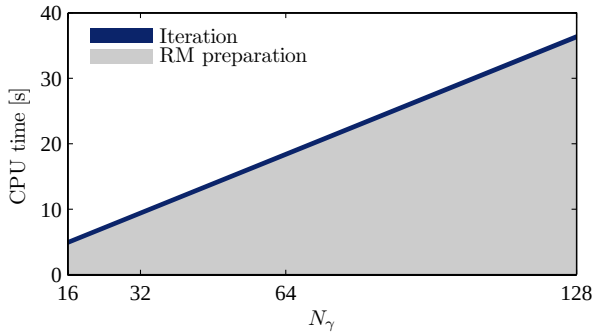

Figure 1.16: CPU times consumed by different N_γ for BEM_3. $N_\alpha = 2$, $N_\beta = 4$

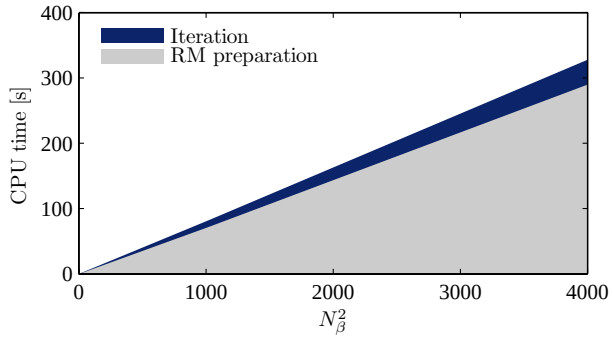

Figure 1.17: CPU times consumed by different N_β for BEM_3. $N_\alpha = 2$, $N_\gamma = 16$

(1.17) and (1.18) shows these relationships. From Figure (1.18) one sees that T_{it} is relatively non-linear versus N_α^2, because n_{cyc} changes from 1876 to 5144 corresponding to N_α from 4 to 28.

Therefore, the total CUP time is the sum of T_{pre} and T_{it}. From Formula (1.39) - (1.41), it is clear how N_α, N_β and N_γ, which are certainly known before a calculation, act on the total CPU time. Thus, it is advisable to choose them properly from the view point of saving CPU time.

At last, T_{it} of BEM_n with $N_\beta = 16$ and $N_\gamma = 64$ is shown in Figure (1.19), as compared with FD and NM algorithms. From the errors on k, it is clear that BEM_3 is the best and BEM_0 is the worst. BEM_2 does not give a better accuracy than BEM_1. In addition, all BEM_n are not competitive with NM but superior to FD.

1.4.3 Summary

From the calculation of a homogeneous core configuration, the factors N_α, N_β and N_γ show complicated features on the accuracy of the k calculation and the corresponding CPU time. On one hand, N_α and N_β directly influence the accuracy of RM for each node and therefore dominate the CPU time for the preparation of RM. One the other hand, N_β and N_γ dominate the accuracy of the critical iteration in multi-nodes calculations. Different order approximations of volume source term give various behaviors. The higher the order, the higher accuracy but the more unstable the iteration process. Above all, BEM_3 is superior to all other models.

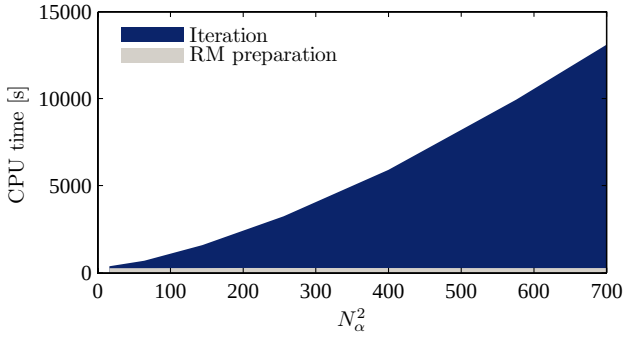

Figure 1.18: CPU times consumed by different N_α for BEM_3. $N_\beta = 32$, $N_\gamma = 64$

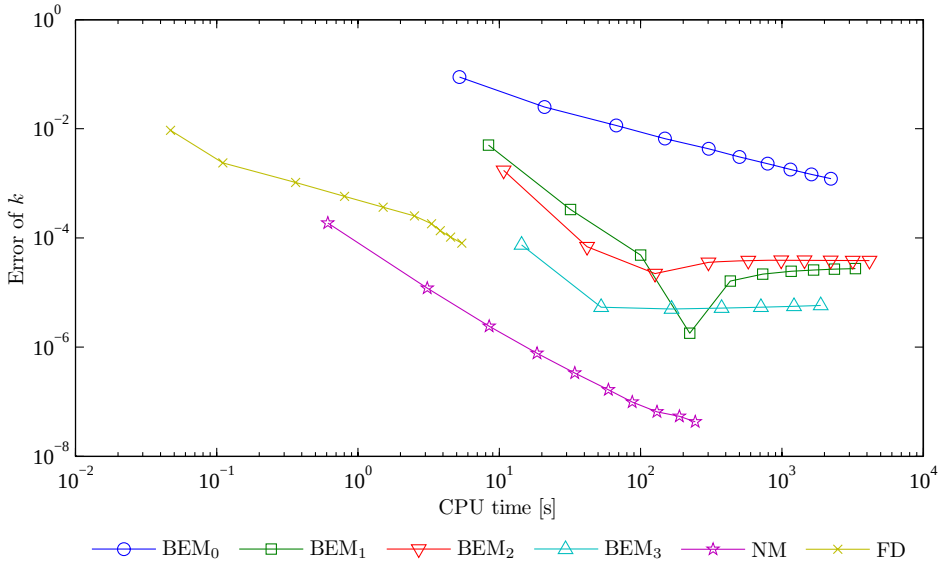

Figure 1.19: Error of k versus CPU times with different N_α. $N_\beta = 16$ and $N_\gamma = 64$ for BEM_n

Chapter 2

Performance and convergence issue of coarse-mesh methods for diffusion calculations

Contributors: Song Han, Sandra Dulla, Piero Ravetto (Politecnico di Torino)

2.1 Introduction

Neutronic calculations for full-core applications are usually based on a coarse-mesh approach to the solution of the multidimensional neutron balance equations. In particular, the nodal method is widely used for full-core evaluation, due to its capability to deal with a geometrically large problem with a reduced computational effort. However, it has been evidenced in past works that the peculiar characteristics of coarse mesh methods can lead in some cases to problems in the convergence of the calculations [1].

The objective of this work is the comparative analysis of coarse-mesh methods for the application to multigroup diffusion [2], starting from standard schemes such as the nodal approach and moving to more innovative options, namely the boundary element method, in order to study the computational performances of these techniques and evidence the possible appearance of non-monotonic convergence problems.

2.2 Coarse-mesh methods

The application of coarse-mesh methods for the solution of the balance equation for neutrons is based on the subdivision of the geometrical domain (i.e. the reactor core) in computational volumes with large dimensions with respect to the spatial scale of the model. This approach allows the reduction of the number of unknowns to deal with in the solution of the neutronic problem; on the other side, some hypotheses on the distribution of the neutron population inside the node have to be made. Material characteristics inside the node are supposed homogeneous and the neutron source due to fission and scattering is expanded in polynomials of a certain order, thus influencing the accuracy of the results obtained.

In the nodal method, the balance equations for neutrons are integrated on the node volume, adopting a polynomial expansion of the internal source, and obtaining numerical relations connecting the incoming current entering the node volume to the corresponding exiting currents. Such relations can be recast

into a response-matrix form, with relevant benefit for the subsequent solution process of the problem. The quality of the results obtained is mainly influenced by the node dimension and by the order of expansion of the source inside the node.

The boundary element method is based on the same coarse-mesh subdivision and response-matrix formulation, but with a different treatment of the neutron balance equation [2, 3]. Quantities defined on the node volume are projected on its boundary and relations for entering and exiting currents are obtained by integration of the corresponding Green function of the problem. This approach allows to reduce the dimensionality of the problem, moving from the node volume to its surface, and the obtained relations can be recast into a response-matrix form . Various parameters influence the accuracy of the numerical evaluation, besides the node dimension and the expansion order of the source as for the nodal method, the number of points defined on the boundary and the algorithm adopted for the integration of the Green function. In particular, this aspect is of crucial importance, since the singular behavior of the diffusion kernel (e.g. Bessel function K_0 in 2D) constitutes a challenging problem for numerical quadrature. This integral may be approached in two ways, by a totally-numerical Gauss-Legendre Quadrature (GLQ) and by a decomposition of the function K_0 in a singular, log-type, portion summed to the regular part of the function. The first one is integrated analytically, while the latter by means of GLQ. Parametric tests show that the semi-analytical approach, even if very accurate on small dimensions, can lack in accuracy for larger nodes, while the numerical approach has stable and more predictable behavior, and is adopted for the following calculations.

The current work is focused on the analysis of the performances of coarse-mesh approaches to the solution of multigroup diffusion problems, with a particular attention to the issue of the convergence of such numerical schemes. In Table 2.1 the methods adopted in the calculations here presented are summarized, together with the most relevant parameters playing a role in the definition of the accuracy of BEM calculations.

Table 2.1: Identification of different numerical methods and characteristic parameters.

ID	Denotation
FD	Finite-Differences
NM	Nodal Method
BEM_n	Boundary Element Method with an nth-order source approximation
N_α	number of nodes along each geometrical dimension
N_β	number of boundary elements used for the discretization of each edge in a node
N_γ	number of Gauss-Legendre Quadrature (GLQ) abscissae

2.3 Selected results

Calculations are performed for one-node and multi-node configurations, using one or three energy groups, and considering system characteristics that allow to obtain an analytical solution to the problem, for benchmark purposes. A numerical solution with a finite-difference code is also provided, in order to compare the performances of coarse-mesh and fine-mesh methods. The finite-difference results can also serve as benchmark reference in most general cases, when no analytical solution is available. As a first step, the case of a two-dimensional single node with 10×10 cm dimensions, in one group diffusion, with reflective boundary conditions on two opposite edges and an incoming current on one edge is considered. The corresponding outgoing current on the opposite edge is the object of the analysis. The medium is considered as purely diffusive and material data are the following: $D = 1.16$ cm and $L^2 = 8$ cm^2. As a consequence no volume source is present and no approximation for its

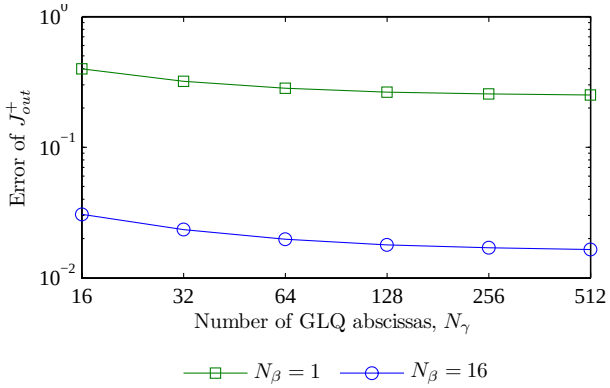

Figure 2.1: One-node calculation with BEM: outgoing current as a function of the number of GLQ abscissae.

integration is introduced. In Fig. 2.1 BEM results are shown, illustrating the behavior of the error on the outgoing current as a function of the number of abscissae adopted for the integral quadrature. Two different discretizations of the boundary (plotted N_β) are considered. It is clearly visible that the refinement of the quadrature formula is providing little improvement to the quality of the results, while the proper discretization of the boundary of the node can serve to reduce the numerical error. The same comments apply to Fig. 2.2, where the same error is depicted as a function of the boundary discretization mesh, for two values of the number of GLQ abscissae.

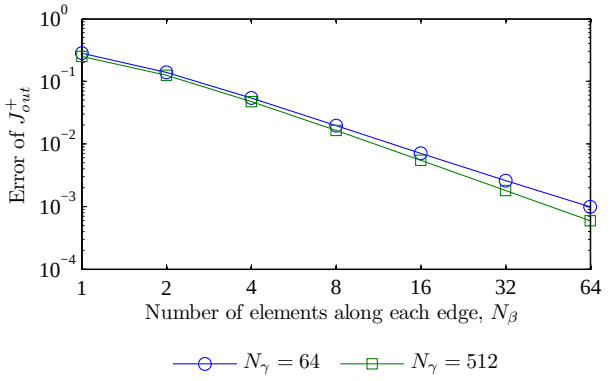

Figure 2.2: One-node calculation with BEM: error on the outgoing current as a function of the number of boundary elements adopted.

A two-dimensional multi-node system, with 160×140 cm dimensions, in three-group diffusion is then considered. Material data are given in Table 2.2. The analytical value of the multiplication constant is $k_{eff} = 0.901454$. The domain is still homogeneous, to allow for analytical comparison, and the k_{eff} of this multiplying structure is evaluated with FD, NM with a third-order expansion within the node and BEM adopting different orders of expansion of the fission source inside the nodes. Comparative results among the different numerical schemes are presented in Table 2.3, where non-monotonic behaviors can be observed. One can see from Table 2.4 the trend of convergence of BEM

Table 2.2: Material data for the homogeneous core

g	Σ_r^g [cm^{-1}]	$\nu\Sigma_f^g$ [cm^{-1}]	D^g [cm]	$\Sigma_s^{g\to 2}$ [cm^{-1}]	$\Sigma_s^{g\to 3}$ [cm^{-1}]	χ^g
1	0.03046	0.01076	2.11	0.02578	0.000516	0.7737
2	0.00706	0.00331	1.29	0.0000	0.004705	0.2193
3	0.00632	0.00437	0.86	0.0000	0.0000	0.0070

Table 2.3: Relative error on criticality eigenvalue with different schemes for the homogeneous, two-dimensional system in three-group diffusion ($N_\beta = 32$, $N_\gamma = 64$).

N_α	BEM_1	FD	NM
4	$4.97719e-3$	$9.28692e-3$	$1.85412e-4$
8	$3.28824e-4$	$2.35108e-3$	$1.15813e-5$
16	$2.14099e-6$	$5.71732e-4$	$3.99355e-7$
32	$2.60024e-5$	$1.34449e-4$	$2.99516e-7$

for increasing orders of approximation. For high values of N_α and low N_β no convergence is reached, at least after 50 cycles. These problems were already observed in past analyses [1] and are characteristics of the coarse-mesh approach. This fact may constitute a serious problem for realistic applications.

Table 2.4: Values of k_{eff} adopting different N_α for BEM_3. Missing values indicate non-converged calculations after 50 iterations with values very far from the correct ones.

N_β	k				
	$N_\alpha = 2$	$N_\alpha = 4$	$N_\alpha = 8$	$N_\alpha = 16$	$N_\alpha = 32$
4	0.900559	0.901057	-	-	-
8	0.898827	0.901364	0.901389	-	-
16	0.898219	0.901391	0.901438	0.901434	-
32	0.898003	0.901389	0.901448	0.901448	0.901448
64	0.897926	0.901385	0.901452	0.901452	0.901452

2.4 Conclusions

The performance of different coarse-mesh approaches is studied at various levels of discretization and for different schemes, including the innovative boundary element technique, within the diffusion model. Problems of convergence may appear in criticality calculations, affecting especially more finely nodalized systems. These irregularities need further investigations to explain mathematical motivations in order to assess the limits of coarse-mesh schemes. In particular, for BEM the interaction between the spatial and boundary discretizations has to be clarified, to establish a consistent scheme for the generation of the mesh.

Bibliography

[1] ZHANG SHAOHONG, LI ZIYONG, Y.A. CHAO, "A Theoretical Study on A Convergence Problem of Nodal Methods," *PHYSOR-2006*, Vancouver (2006).

[2] HAN SONG, S. DULLA, P. RAVETTO, "Computational methods for multidimensional neutron diffusion problems," *Science and Technology of Nuclear Installations*, DOI: 10.1155/2009/973605 (2009).

[3] M. MAIANI, M. MONTAGNINI, "A boundary element-response matrix method for the multigroup neutron diffusion equations," *Annals of Nuclear Energy*, **26**, 1341-1369 (1999).

Chapter 3

Development of dynamic models for neutron transport calculations

Contributors: Fabio Alcaro, Sandra Dulla, Piero Ravetto (Politecnico di Torino), Guy Marleau (Ecole Polytechnique de Montréal), Ernest Mund (Université Libre de Bruxelles)

3.1 Introduction

For several applications in the physics of nuclear systems an accurate transport model may be needed to adequately describe the evolution of the neutron population in perturbed conditions. This may be the case especially when treating advanced systems, such as source-driven subcritical assemblies or some of the Generation IV reactor configurations. In such systems, the use of diffusion models cannot fully account for important physical phenomena.

A direct approach involves the inversion of the transport operator on a very short time scale, thus implying a huge computational effort. To overcome this problem, the quasi-static method can be very appropriate, allowing to obtain high-quality time-dependent predictions with a reasonable computational effort.

In this work, a computational tool coupling the existing transport code DRAGON to a kinetic module is described. The transport code is used for the generation of the shapes needed to evaluate the kinetic parameters of the amplitude model, which is solved on a fast time scale. Two possible implementations of the quasi-static scheme are considered: the Improved Quasi-static Method (IQM) and the Predictor-Corrector Quasi-static Method (PCQM). Some test results are presented and discussed.

3.2 Quasi-static approaches to the time-dependent transport problem

The time-dependent analysis of nuclear systems requires the solution of the balance equations for neutrons and delayed neutron precursors:

$$\begin{cases} \dfrac{1}{v}\dfrac{\partial\varphi}{\partial t} = \mathscr{L}(t)\varphi(t) + \dfrac{1}{4\pi}\displaystyle\sum_{i=1}^{I}\chi_i(E)\lambda_i C_i(\boldsymbol{r},t) + S(\boldsymbol{r},E,\boldsymbol{\Omega},t), \\ \dfrac{\chi_i(E)}{4\pi}\dfrac{\partial C_i}{\partial t} = -\dfrac{\chi_i(E)}{4\pi}\lambda_i C_i(\boldsymbol{r},t) + \mathscr{F}_i^d(t)\varphi(t), \qquad i=1,2,\ldots,I, \end{cases} \tag{3.1}$$

where $\varphi(t) \equiv \varphi(\boldsymbol{r}, E, \boldsymbol{\Omega}, t)$ and $C_i \equiv C_i(\boldsymbol{r}, t)$ denote the neutron angular flux and the delayed neutron precursors concentrations, respectively. The general definitions of the operators appearing in Eqs. (3.1) is well-known and can be found in ref. [1].

Since the complete solution of system (3.1) is highly computer-time consuming, various approximate models for neutron kinetics have been developed during the past years [2, 3, 4, 5, 6]. In particular, the quasi-static approach is based on the factorization of the neutron flux in the product of an amplitude function A, only depending on time, and a shape function ψ, depending on the phase space variables and, on a slower time scale, on time:

$$\varphi(\boldsymbol{r}, E, \boldsymbol{\Omega}, t) = A(t)\psi(\boldsymbol{r}, E, \boldsymbol{\Omega}; t). \tag{3.2}$$

The introduction of the factorization formula (3.2) into the balance equations (3.1) leads to what is referred to as *shape model*:

$$\begin{cases} \dfrac{1}{v}\dfrac{\partial \psi}{\partial t}A + \dfrac{1}{v}\dfrac{dA}{dt}\psi = \mathscr{L}(t)\psi(t)A(t) + \dfrac{1}{4\pi}\displaystyle\sum_{i=1}^{I}\chi_i(E)\lambda_i C_i(\boldsymbol{r}, t) + S(\boldsymbol{r}, E, \boldsymbol{\Omega}, t), \\ \dfrac{\chi_i(E)}{4\pi}\dfrac{\partial C_i}{\partial t} = -\dfrac{\chi_i(E)}{4\pi}\lambda_i C_i(\boldsymbol{r}, t) + \mathscr{F}_i^d(t)\psi(t)A(t), \qquad i = 1, 2, \ldots, I. \end{cases} \tag{3.3}$$

The factorization introduced, Eq. (3.2), is general and thus non-unique. A normalization constraint is introduced requiring the integral of the neutron density, weighted on the adjoint function associated to a reference initial configuration, to be constant:

$$\left\langle \psi_0^\dagger, \frac{1}{v}\psi \right\rangle := \int d\boldsymbol{r} \int dE \oint d\boldsymbol{\Omega}\, \psi_0^\dagger(\boldsymbol{r}, E, \boldsymbol{\Omega})\frac{1}{v}\psi(\boldsymbol{r}, E, \boldsymbol{\Omega}, t) = \gamma_0 \equiv \left\langle \psi_0^\dagger, \frac{1}{v}\varphi_0 \right\rangle, \tag{3.4}$$

where φ_0 is the neutron flux in the initial configuration. This choice is convenient, since the following step consists in the projection of the shape model over the same weighting function, taking advantage of the simplification introduced by condition (3.4), obtaining the *amplitude model*:

$$\begin{cases} \dfrac{dA}{dt} = \dfrac{\rho(t) - \tilde{\beta}(t)}{\Lambda(t)}A(t) + \displaystyle\sum_{i=1}^{I}\lambda_i \tilde{c}_i(t) + \tilde{S}(t) \\ \dfrac{d\tilde{c}_i}{dt} = -\lambda_i \tilde{c}_i(t) + \dfrac{\tilde{\beta}(t)}{\Lambda(t)}A(t), \qquad i = 1, 2, \ldots, I. \end{cases} \tag{3.5}$$

When the shape function is equal to the steady-state initial neutron flux φ_0, the point kinetic equations (PK) are derived.

Both the shape and amplitude models are non-linear, since the kinetics parameters in (3.5) depend on the shape and the product of the two unknowns appears explicitly in (3.3). The Improved Quasi-static Method (IQM) takes advantage of the different time scales appearing in the transient evolution. First, the amplitude equations are solved over a large time interval Δt, using a finer time mesh δt. Then, the shape model is solved on the same Δt, updating the kinetic parameters and iterating the solution by modifying the derivative of the amplitude function. This allows to reduce the error on the normalization condition (3.4), defined as:

$$\varepsilon_\gamma = \frac{|\gamma - \gamma_0|}{\gamma_0}, \qquad \gamma = \left\langle \psi_0^\dagger, \frac{1}{v}\psi \right\rangle. \tag{3.6}$$

The block diagram for IQM is sketched in Fig. 3.1a, enlightening the presence of the normalization iterations. The non-linearity of IQM can represent a relevant problem, since the convergence of the γ parameter is a critical aspect. For this reason, a different approach to quasi-statics has been recently

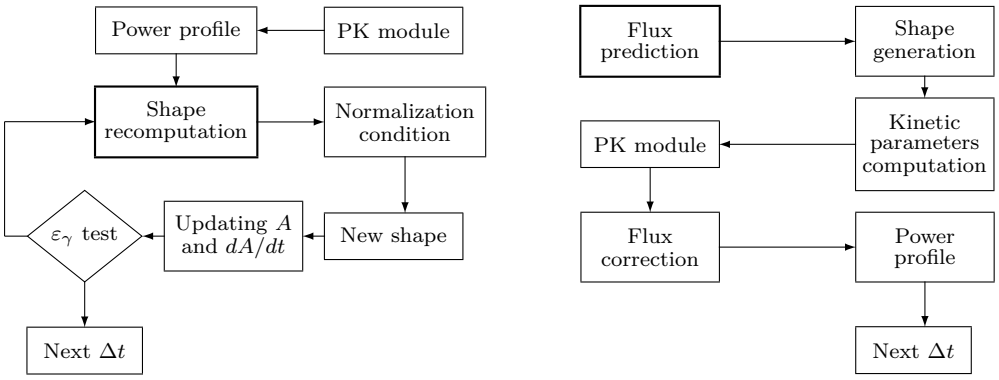

(a) IQM. (b) PCQM.

Figure 3.1: Block diagram of the quasi-static algorithms for a single Δt computation. Bold-edged boxes identify tasks demanded to the DRAGON code.

proposed to overcome this issue, the Predictor-Corrector Quasi-static Method (PCQM) [1, 7]. The two time-scale approach to the time-dependent problem is still used, but the shape update procedure is carried out first to obtain improved kinetic parameters. To do so, the neutron balance equations (3.1) are solved on the coarse time step Δt and the obtained predicted flux is renormalized in order to obtain a shape fulfilling condition (3.4). The kinetic parameters evaluated with the new shape are then used for the solution of Eqs. (3.5), to provide the power evolution on the fine mesh δt. The block diagrams for PCQM is given in Fig. 3.1b.

3.3 Description of the work

The quasi-static algorithms described in the previous section require the solution of a time-dependent balance equation for neutrons and precursors. Once the time derivative is approximated by a suitable numerical scheme, both the neutron balance equations (3.1) and the shape model (3.3) can be recast into a pseudo-stationary form. In this work, a first-order Implicit-Euler scheme is adopted. The shape model for IQM can be written as:

$$\left[\mathscr{L}(t) - \frac{1}{v\Delta t} - \frac{1}{vA(t)}\frac{dA}{dt}\right]\psi(\boldsymbol{r}, E, \boldsymbol{\Omega}, t) + \tilde{Q}(\boldsymbol{r}, E, \boldsymbol{\Omega}, t) = 0, \tag{3.7}$$

where the generalized source $\tilde{Q}$, including the contribution of precursors, takes the form:

$$\begin{aligned}\tilde{Q}(\boldsymbol{r}, E, \boldsymbol{\Omega}, t) = \frac{S(\boldsymbol{r}, E, \boldsymbol{\Omega}, t)}{A(t)} + \frac{\psi(\boldsymbol{r}, E, \boldsymbol{\Omega}, t - \Delta t)}{v\Delta t} + \sum_i \lambda_i \frac{\chi_i}{4\pi}\frac{1}{A(t)} \\ \cdot \left[C_{i,0}(\boldsymbol{r})e^{-\lambda_i \Delta t} + \int_{t-\Delta t}^{t} d\tau \mathscr{F}_i^d(\tau)\varphi(\boldsymbol{r}, E, \boldsymbol{\Omega}, \tau)e^{-\lambda_i\left(t-\tau\right)}\right],\end{aligned} \tag{3.8}$$

and a time-absorption term, depending on the value of the amplitude and its derivative, appears on the left-hand-side of (3.7).

In PCQM, the form of the pseudo-stationary equation is:

$$\left[\mathscr{L}(t) - \frac{1}{v\Delta t} + \frac{\Delta t}{2}\sum_i \lambda_i \mathscr{F}_i^d(t)\right]\tilde{\varphi}(\boldsymbol{r}, E, \boldsymbol{\Omega}, t) + \tilde{Q}(\boldsymbol{r}, E, \boldsymbol{\Omega}, t) = 0, \tag{3.9}$$

where the generalized source $\tilde{Q}$ is now defined as:

$$\begin{aligned}\tilde{Q}(\boldsymbol{r}, E, \boldsymbol{\Omega}, t) = S(\boldsymbol{r}, E, \boldsymbol{\Omega}, t) + \frac{\psi(\boldsymbol{r}, E, \boldsymbol{\Omega}, t - \Delta t)}{v\Delta t} \\ + \sum_i \lambda_i \left[\frac{\chi_i}{4\pi} C_{i,0}(\boldsymbol{r}) e^{-\lambda_i \Delta t} + \frac{\Delta t}{2}\mathscr{F}_i^d(t)\tilde{\varphi}(\boldsymbol{r}, E, \boldsymbol{\Omega}, t)\right].\end{aligned} \tag{3.10}$$

This feature of both approaches is well suited for the use of a steady-state solver instead of a full dedicated time-dependent code. This possibility allows to use well-assessed and optimized flux solvers to be coupled to an external module dealing with the quasi-static algorithms [8].

In this work, the open-source stand-alone steady-state neutron transport solver DRA-GON, developed by the École Polytechnique de Montréal, is used [9]. The code is coupled to a kinetic module, implementing the quasi-static schemes described before, through an interface module which manages the Input/Output data. Equations (3.7) and (3.9) are solved introducing *virtual* cross-sections and sources in the transport solver. The quasi-static procedure is established through linked computational modules.

3.4 Results

In this section some test calculations are presented in order to demonstrate the feasibility of the procedure and the efficiency of the computational tool in the prediction of the reactor power evolution, induced by source and cross-section perturbations inserted into the system. However, it must be highlighted that, in order to obtain a fully consistent model with Eqs. (3.8) and (3.10), the steady-state transport solver must accept angular-dependent sources and provide angular fluxes as output, for the computation of the kinetic parameters. In this work, the DRAGON code solves the transport equation using the collision probability method, with a 10^{-6} maximum tolerance on the error on the eigenvalue and the flux. This module provides as output the scalar fluxes and accepts as input only isotropic source distributions. These aspects constitute an inconsistency in the formulation of the quasi-static algorithm and could introduce relevant errors when problems with a high anisotropy are concerned (e.g. high-energy neutrons). However, the results in the current section show that for some cases accurate power predictions can be obtained.
The dynamic code takes into account the presence of delayed neutrons. The choice of macro Δt and micro δt time-step sizes is provided by the user. In the following calculations $\delta t = 10^{-6}$ s, while parametric studies on the value of Δt are performed. In Fig. 3.2, a picture of the two systems analyzed is presented. They are adopted for one-group and three-group calculations, respectively.

As a preliminary assessment, a transient induced by doubling the external neutron source intensity is considered for the system in Figure 3.2a. The transport problem being linear, the final value of the power must be consequently doubled. Results are presented in Fig. 3.3. The presence of delayed neutrons is taken into account by considering one family of precursors only, with $\beta = 500$ pcm and $\lambda = 100$ s^{-1}. This value of the decay constant, even if not realistic, allows to analyze whether the code is treating correctly the presence of precursors and the consequent different time scales, adopting a reduced transient duration. The convergence to the asymptotic solution can be clearly seen.

The study of test transients involving delayed neutron precursors points out a main difference between IQM and PCQM: the presence of delayed neutrons requires to adapt the macro time-step along

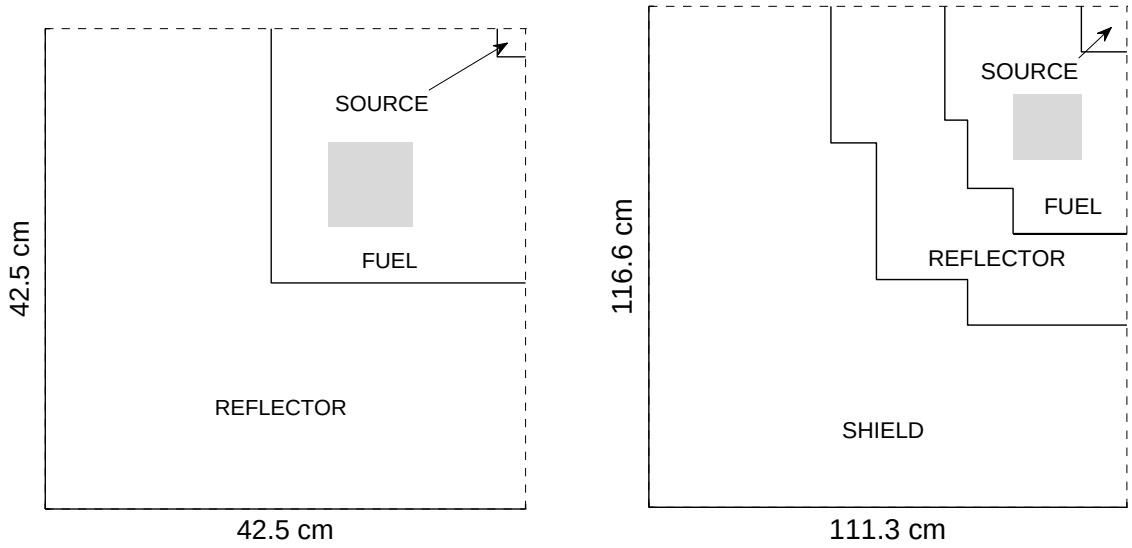

(a) 2D square test reactor.

(b) 2D MASURCA-like reactor.

Figure 3.2: Representation of one quarter of the two reactor domains. The shaded areas identify the regions where cross-section perturbations are introduced. The neutron transport calculations are performed by imposing reflective boundary conditions on the dashed edges, while vacuum boundary conditions are imposed on the solid edges.

the evolution of the transient to capture the change of the neutron shape. If an adaptive technique is considered, it can be assumed that, once the spatial transient is extinguished, the following evolution up to equilibrium with the delayed neutron precursors (last Δt) could be well retraced by a PK calculation with the last available kinetic parameters. In IQM this is automatically fulfilled, since the amplitude calculation is performed before the shape update. On the other hand, PCQM requires as a first step the solution of the flux problem, which can lead to significant errors when the last Δt is too large. To overcome this problem, the PCQM should be hybridized with a PK module that performs the calculation along the last Δt.

A second test calculation carried out for the system in Fig. 3.2a is a transient induced by a step-wise fission cross section perturbation, leaving the reactor in a subcritical state. The same data for precursors as in the previous case are assumed. Since after a transient the system settles on a new steady-state, an asymptotic transport calculation is carried out to determine the *exact* value of the flux and of the power at the end of the transient. It is clear from Figs. 3.4 and 3.5 that a correct evaluation of the power evolution requires the analysis up to the time when delayed neutrons reach equilibrium. Moreover, a full PK treatment is not sufficient to predict the power level at the end of the transient, while both IQM and PCQM can provide accurate results.

In Fig. 3.6 a test calculation for the system in Fig. 3.2b is presented. For the sake of simplicity, no delayed neutrons are considered, in order to reduce the time interval on which the analysis is carried out. It can be observed that IQM requires a certain number of shape updates to provide a satisfactory power prediction. This is due to the error introduced in the shape recomputation process. On the other hand, PCQM can produce reliable results even considering just one macro time-step, provided it is short enough. Nevertheless, in most calculations, the shape recomputation error introduced in the IQM does not affect dramatically the power prediction, as it is usually of the order of the relative

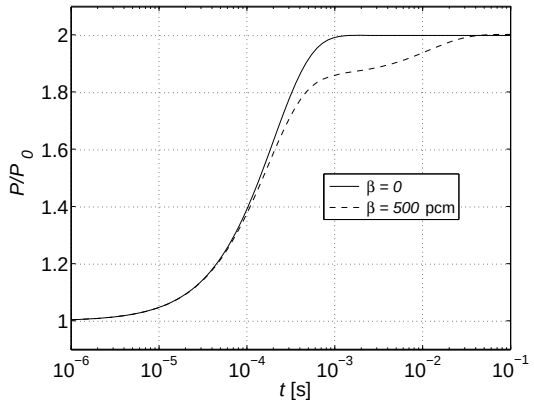

Δt [ms]	IQM	PCQM
5.00	2.000275	2.000333
2.50	2.000371	2.000469
1.25	2.000480	2.000480
1.00	2.000540	2.000539

Figure 3.3: Doubling of the external source. The values in the table refer to the power levels at the end of the transient, in the case without delayed neutrons. The macro time-steps and the micro time-steps are uniform.

error on the power itself.

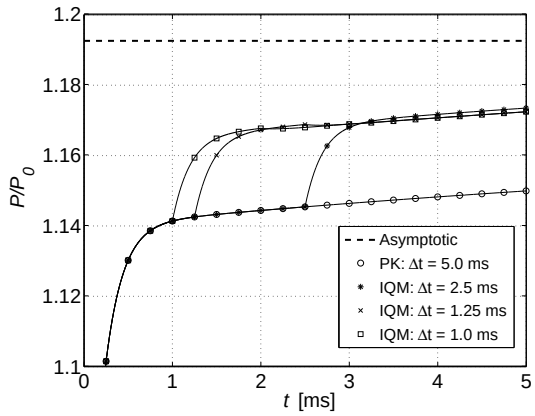

(a) Comparison of the power evolution for IQM. The time interval is subdivided into uniform macro time-steps.

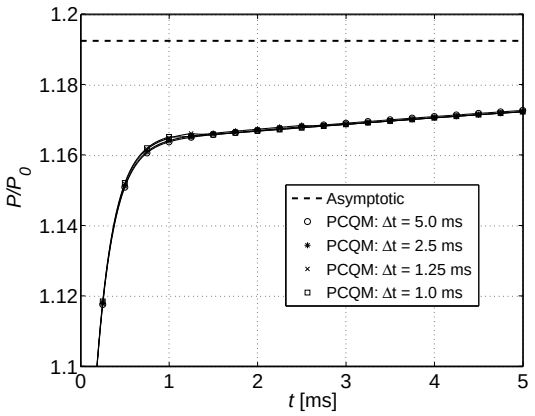

(b) Comparison of the power evolution for PCQM. The time interval is subdivided in uniform macro time-steps.

Figure 3.4: Power evolution induced by a uniform fission cross-section perturbation ($\delta\nu\Sigma_f/\nu\Sigma_f = +10\%$). The initial multiplication factor is 0.96884. The reactivity insertion is $\Delta\rho = +574$ pcm. The graph is zoomed in the region $[0, 5$ ms$]$, to evidence the prompt-jump.

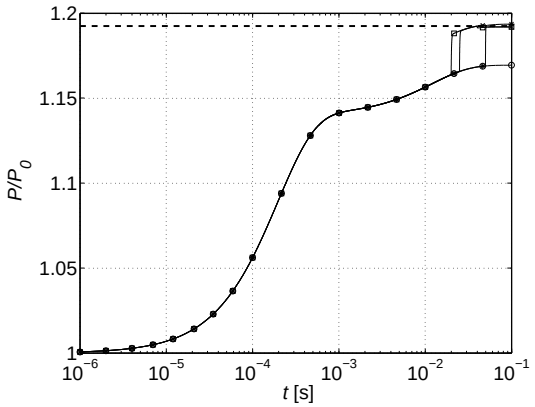

(a) Comparison of the power evolution for the whole transient analysis adopting the IQM. Markers as in Fig. 3.4a

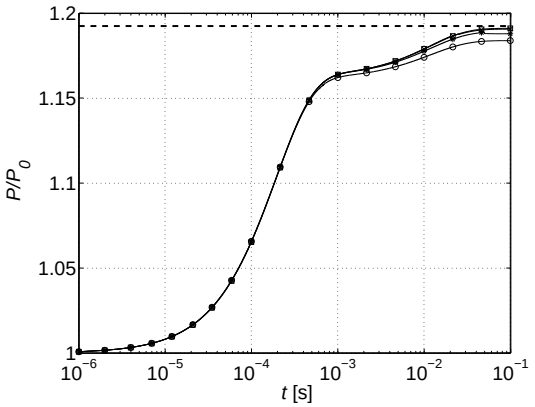

(b) Comparison of the power evolution for the whole transient analysis adopting the PCQM. Markers as in Fig. 3.4b

Figure 3.5: Power evolution for the full transient. The time interval is subdivided in uniform macro time-steps, the same for both IQM and PCQM.

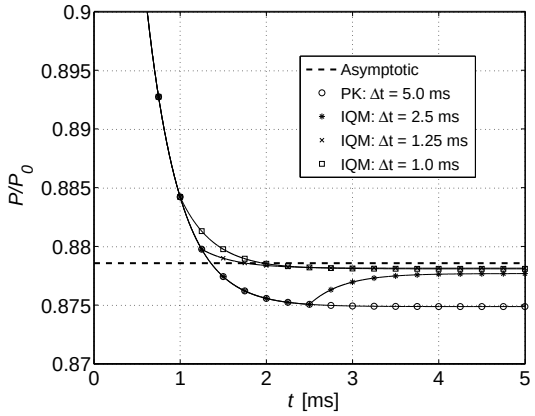

(a) Comparison of the power evolution for IQM.

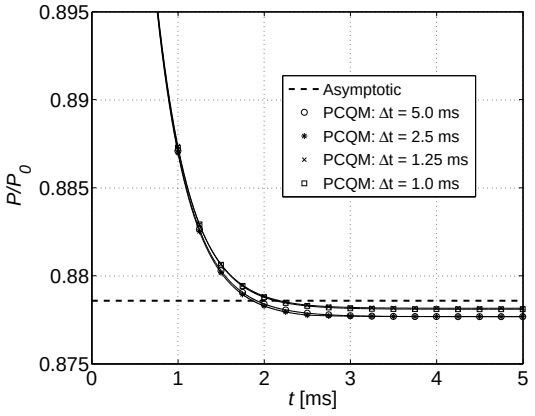

(b) Comparison of the power evolution for PCQM.

Figure 3.6: Power evolution induced by a uniform capture cross-section perturbation ($\delta\Sigma_c/\Sigma_c = +20\%$). The initial multiplication factor is 0.97240. The reactivity insertion is $\Delta\rho = -371$ pcm. The view is zoomed in the region $[0, 5$ ms$]$, where only the prompt neutron equilibrium is reached.

3.5 Conclusions

A computational tool that can perform time-dependent neutronic transport calculations using a quasi-static approach is developed. The DRAGON code is used as a transport solver to generate direct and adjoint fluxes, to be used for the calculation of the kinetic parameters introduced into the amplitude model. A coupling module provides the input information for the DRAGON code by suitable modifications of cross sections and sources as needed, in order to take into account the evolution of neutron and precursor concentrations.

Test calculations show the feasibility of the procedure and the accuracy of the results, both for the classical IQM and for the innovative PCQM. Some considerations are highlighted concerning the possibility to hybridize the two algorithms when dealing with a long transient analysis. The results presented show that both algorithms can reproduce the power level at the end of the transient rather accurately: it must be reminded that PCQM is computationally more advantageous than IQM.

Further development should be directed towards handling angular distributions for sources and fluxes. This step will lead to a fully consistent computational tool for transport nuclear reactor kinetics.

Bibliography

[1] Dulla S., Mund E.H., Ravetto, P., The quasi-static method revisited, *Progress in Nuclear Energy*, **50**,908–920, 2008.

[2] Henry A.F., The Application of Reactor Kinetics to the Analysis of Experiments, *Nuclear Science and Engineering*, **3**, 52–70, 1958.

[3] Yasinsky J.B., Henry A.F., Numerical Experiments Concerning Space-Time Reactor Kinetics Behavior, *Nuclear Science and Engineering*, **22**, 171–181, 1965.

[4] Ott K.O., Meneley D.A., Accuracy of the Quasistatic Treatment of Spatial Reactor Kinetics, *Nuclear Science and Engineering*, **36**, 402–411, 1969.

[5] Devooght J., Quasistatic Solutions of Reactor Kinetics, *Annals of Nuclear Energy*, **7**, 47–58, 1980.

[6] Devooght J., Mund E.H., Generalized Quasistatic Method for Space-time Kinetics, *Nuclear Science and Engineering*, **76**, 10–17, 1980.

[7] Dulla S., Mund E.H., Ravetto, P., Accuracy of a Predictor-Corrector Quasi-Static Method for Space-Time Reactor Dynamics, *PHYSOR'06*, Vancouver, 2006.

[8] Picca P., Dulla S., Mund E.H., Ravetto P., Marleau G., Quasi-static Time-Dependent Computational Tool Using the DRAGON Transport Code, *PHYSOR'08*, Interlaken, 2008.

[9] Marleau G., Hébert A., Roy R., A user's guide for DRAGON 3.05, *Report IGE-174 Rev. 6*, Institut de Génie Nucléaire, Ecole Polytechnique de Montréal, 2006.

[10] Eriksson M., Accelerator-driven Systems: Safety and Kinetics, *PhD thesis*, Royal Institute of Technology, Stockholm, 2005.